

Dicke's Superradiance in Astrophysics. I – The 21 cm Line

Fereshteh Rajabi¹ and Martin Houde^{1,2}

¹*Department of Physics and Astronomy, The University of Western Ontario, London, ON, N6A 3K7, Canada*

²*Division of Physics, Mathematics and Astronomy, California Institute of Technology, Pasadena, CA 91125, USA*

Abstract

We have applied the concept of superradiance introduced by Dicke in 1954 to the ISM by extending the corresponding analysis to the magnetic dipole interaction characterizing the atomic hydrogen 21 cm line. Although it is unlikely that superradiance could take place in thermally relaxed regions, in situations where the conditions necessary for superradiance are met (i.e., close atomic spacing, high velocity coherence, population inversion, and long dephasing time-scales compared to those related to coherent behavior), our results suggest that relatively low levels of population inversion over short astronomical length-scales (e.g., as compared to those required for maser amplification) can lead to the cooperative behavior required for superradiance in the ISM. Given the results of our analysis, we expect the observational properties of superradiance to be characterized by the emission of high intensity, spatially compact, burst-like features potentially taking place over short periods ranging from minutes to days.

Subject headings: atomic processes – ISM: atoms – radiation mechanisms: general

1. Introduction

It is generally assumed that in much of the interstellar medium (ISM) emission emanating from atomic and molecular transitions within a radiating gas happen independently for each atom or molecule. From intensity measurements of such spectral lines, important parameters (e.g., density and temperature) can be determined and the physical conditions in a given environment thus characterized (Townes et al. 1955; Emerson 1996; Goldsmith et al. 1999; Irwin 2007). For example, in cases where the spectral lines are optically thin the intensity will be found to scale linearly with the number of atoms or molecules responsible for the detected radiation. The soundness of this approach rests mostly on the assumption that spontaneous emission from different atoms or molecules happens independently.

As was pointed out by R. H. Dicke in a seminal paper several decades ago (Dicke 1954), the assumption of independent spontaneous emission for the components of a gas does not apply in all

conditions. As will be discussed in this paper, and following Dicke’s original analysis, closely packed atoms can interact with their common electromagnetic field and radiate coherently. That is, the spontaneous emission of atoms or molecules in such a gas will not be independent, but rather take place in a cooperative manner. In the ideal case, this phenomenon will lead to a much more intense and focussed radiation (proportional to the square of the number of atoms), which Dicke called superradiance. Since Dicke’s original proposal, the field of superradiance research has flourished and an abundant literature has developed within the physics community. The first experimental detection of superradiance in the laboratory was achieved by Skribanowitz et al. (1973), while several other independent verifications (Gross et al. 1976; Gibbs et al. 1977; Carlson et al. 1980; Moi et al. 1983; Greiner et al. 2000; Xia et al. 2012) have since been realized under a large domain of conditions and experimental setups (see Chap. 2 of Benedict et. al. 1996; MacGillivray & Feld 1976; Andreev et al. 1980; Gross & Haroche 1982 for reviews).

While the reality of the superradiance phenomenon has long been clearly established in the laboratory, to the best of our knowledge, it has yet to be investigated within an astrophysical context. It appears to us important to do so since some of the requirements and conditions needed for the realization of a superradiant system are known to be satisfied in some regions of the ISM. More precisely, superradiance can arise in systems where there is a population inversion, and the effect will be much stronger and more likely to be realized when atoms or molecules are separated by approximately less than the wavelength of radiation (see below and Section 3.3).

The population inversion condition is known to occur in the ISM and is partly responsible for the ubiquitous presence of masers (see Fish 2007; Watson 2009; Vlemmings 2012; Sarma 2012 for recent reviews). But it is also important to realize that, although it is a necessary condition, population inversion is not by itself sufficient to ensure superradiance. It is also required that there exists sufficient velocity coherence between the atoms partaking in the effect, and that any other dephasing takes place on time-scales longer than those characterizing superradiance. When all these conditions are met a coherent behavior can be established between the atoms and superradiance can ensue. We note, however, that, as will be discussed later on, it is unlikely that superradiance could take place in thermally relaxed regions of the ISM. This is because Doppler broadening resulting from, say, a Maxwellian velocity distribution would leave too few atoms with the required velocity coherence to allow superradiance to develop. Our analysis will therefore imply other types of environments where thermal equilibrium has not been reached. For example, any region in the ISM into which a significant amount of energy is being suddenly released (e.g., shocks or regions where significant radiation flares occur) will be strongly out of equilibrium, and provide conditions that are potentially markedly different to those found in a thermal gas and may meet the requirements for superradiance. Also, although superradiance can also occur for large interatomic or molecular separations (i.e., greater than the wavelength of radiation; see Section 3.2.2), the aforementioned constraint of small interatomic or molecular separation, and its implication for the corresponding densities, is likely to be met for only a limited number of spectral lines, but a few astrophysically important transitions are suitable candidates. One of these spectral lines is the 21 cm atomic

hydrogen transition.

Even though a 21 cm maser has yet to be discovered, which would also imply the realization of a population inversion for this spectral line, as will be seen through our analysis the length-scales required for superradiance at 21 cm are very small compared to those that would be needed for maser amplification in the ISM (Storer & Sciama 1968, and see below). It follows that the absence of masers for this transition does not rule out the possibility of superradiance. Also, the existence of higher densities of atomic hydrogen in some parts of the ISM would increase the potential detectability of superradiance, if the other necessary conditions for its realization previously listed were also met. Furthermore, with the recent discoveries of radio bursts at frequencies close to 1400 MHz (Kida 2008) the investigation of the properties of a transient phenomenon such as superradiance is timely. This is why in this first paper on the subject we chose to introduce the concept of superradiance to the ISM using this spectral line.

Whether or not a population inversion can easily be realized for the energy levels leading to the 21 cm line is admittedly unclear, but it has been considered in the existing literature (Shklovskii 1967; Storer & Sciama 1968; Dykstra & Loeb 2007) and we know of at least one region (the Orion Veil) where the kinetic temperature is lower than the 21 cm spin temperature, implying a population inversion (Abel et al. 2006). The main pumping process covered in the literature corresponds to the situation when a HI gas is close to a source of radiation that emits a field with an intensity $I_v(\nu)$ in the neighborhood of the Lyman α line. A hydrogen atom in the ground hyperfine state ($n = 1, F = 0$) can absorb a photon and become excited to the $n = 2$ level. Later on, the atom returns to the upper hyperfine state ($n = 1, F = 1$) emitting a slightly less energetic photon than the initial one absorbed by the atom. The same can happen for a hydrogen atom initially in the hyperfine state ($n = 1, F = 1$) that returns to the ground ($n = 1, F = 0$) state after excitation to the $n = 2$ level, emitting a slightly more energetic photon in the process. The absorption rate of the photons for both cases depends on the intensity of the radiation $I_v(\nu)$, but the return (emission) process does not. Therefore, the $F = 0$ level will undergo more absorptions followed by a return to the ($n = 1, F = 1$) level whenever $I_v(\nu)$ harbors more blue than red photons, and will become accordingly less populated than the $F = 1$ level (Field 1958; Shklovskii 1967; Storer & Sciama 1968). Although Storer & Sciama (1968) concluded that it is unlikely to maintain a population inversion over an extended region needed for the maser amplification with this process, they also pointed out that an “appreciable” inversion can thus be realized over a region of thickness $\sim 6 \times 10^{-5}$ pc. Given the above inversion scenario, we would expect that environments located in the periphery or near boundaries of HII regions could provide conditions suitable for the development of superradiance, for example. The aforementioned presence of a 21 cm population inversion in the Orion Veil brings support to this idea. Whatever the case, the 21 cm line will serve us as a starting point for the development of the superradiance formalism for the ISM (in the present case for a magnetic dipolar transition), which will then be refined in the future and also applied to another (electric dipolar) spectral line in our second paper on the subject (Rajabi & Houde 2016).

It should also be pointed out that superradiance is a fundamentally different phenomenon from

a maser, even though the two may seem similar at first glance. An astronomical maser is a collective but not coherent phenomenon. More precisely, for a maser a group of atoms, initially in their excited states, emit through the stimulated emission process but cannot be considered as a single quantum system. That is, it is possible to describe maser action through successive events where an excited atom is stimulated by the incident radiation and emits a photon, with the same stimulation/emission processes subsequently repeated for different atoms in the maser sample. On the other hand for superradiance, coherence emphasizes the fact that the group of atoms interacting with the radiation field behaves like a single quantum system (Nussenzveig 1973). That is, the superradiance emission process cannot be broken down into successive events as is the case of maser radiation. Finally, superradiance is a transient effect in which a strong directional pulse is radiated over a relatively short time-scale, while maser operates more in a steady state regime as long as population inversion is maintained.

The material covered in this paper goes as follows, we start with a brief and general discussion of the concept of superradiance for the so-called small- and large-samples, as originally discussed by Dicke (1954, 1964), in Section 2. In Section 3, we develop the superradiance formalism for, and examine the possibility of building cooperative behavior in, a HI sample based on a comparative analysis of time-scales for the 21 cm line for a HI gas in the ISM, as well as present corresponding numerical results. A discussion and short conclusion follow in Sections 4 and 5, respectively, while appendices providing detailed calculations for the material discussed in the main sections of the paper will be found at the end.

2. Superradiance

2.1. Dicke’s Small-sample Model

Dicke originally proposed in 1954 a model where an ensemble of N initially inverted two-level atoms interacting with their common radiation field is considered as a single quantum mechanical system (Dicke 1954). In his model, a two-level atom is modeled as a spin-1/2 particle in a magnetic field where the spin up configuration corresponds to the excited state $|e\rangle$ and the spin down to the ground state $|g\rangle$. Just as an ensemble of N spin-1/2 particles can be described using two quantum numbers s and m_s , the eigenstates of the combined N two-level atoms in Dicke’s model can also be labelled with two quantum numbers r and m_r such that $0 \leq r \leq N/2$ and $m_r = -r, -r + 1, \dots, r - 1, r$, where

$$m_r = \frac{N_e - N_g}{2}, \quad (1)$$

with N_e and N_g the number of particles in the excited and ground states, respectively. From the complete set of eigenstates characterizing this quantum mechanical system, those symmetrical under the permutation of any pair of atoms are particularly important and are called Dicke states. The initial state $|e, e, \dots, e\rangle$ of N fully inverted spin-1/2 particles corresponding to N fully inverted two-

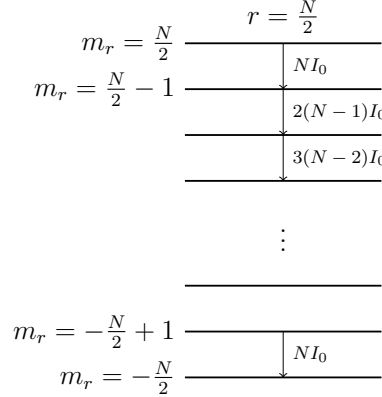


Fig. 1.— Dicke states with $r = N/2$ for a system of N two-level (spin-1/2) particles. Spontaneous radiation intensities are indicated on the right.

level atoms is one such Dicke state, and is identified by $r = N/2$ and $m_r = N/2$. When an atom in the ensemble decays to its ground state by emitting a photon, the quantum number m_r is decreased by one while r remains unchanged and the system moves to another symmetric state. Dicke showed that the radiation intensity from such an ensemble cascading from the initial ($r = N/2$, $m_r = N/2$) state down through an arbitrary state (r , m_r) is

$$I = I_0 (r + m) (r - m + 1) \quad (2)$$

if the volume containing the ensemble of N two-level atoms is much smaller than λ^3 , the cube of the wavelength of the radiation interacting with the atoms. In Equation (2), I_0 is the radiation intensity due to spontaneous emission from a single two-level atom. This particular type of system and density condition defines a *small-sample*. This cascading process is depicted in Figure 1.

Furthermore, Dicke pointed out that in the ($r = N/2$, $m_r = 0$) state, where the half of the atoms are in the ground state and the other half in the excited state, the radiation intensity of the system is maximum at

$$I = I_0 \left(\frac{N}{2} \right) \left(\frac{N}{2} + 1 \right) \quad (3)$$

$$\propto N^2 I_0, \quad (4)$$

implying a significantly enhanced radiation beam, a phenomenon he named *superradiance*. This can be understood by the fact that when the distance between neighboring atoms is much smaller than the wavelength of radiation, the photon emitted by one atom is seen to be in phase by neighboring atoms and can bring about the emission of a new photon of the same mode and the same direction as the initial photon. This process can continue through the whole ensemble resulting in an intense

superradiant radiation pulse proportional to N^2 (see Equation [4]). In contrast to superradiance observed in a perfectly coherent system, in a non-coherent system all atoms act independently with a radiation intensity scaling linearly with N . This possibility of coherent interactions is in contrast with the common assumption that in the ISM atoms, for example, mainly interact independently with the radiation field, such that the intensity of the radiation is a linear function of the atomic density.

In order to conduct a more careful investigation of the possibility of coherent interactions, especially superradiance in a HI gas, we will need to adapt Dicke's original theory to the corresponding conditions in the ISM. We therefore first need to carefully understand all the assumptions that lead to a symmetrical ensemble and superradiance in the original model of Dicke (1954). The main assumptions can be listed as follows:

- A small-sample of neutral atoms is confined to a volume $\mathcal{V} \ll \lambda^3$ with the walls of the volume transparent to the radiation field.
- The N two-level atoms in the sample are separated by a distance much less than λ but distant enough not to worry about any overlap between the wave functions of neighboring atoms, which would require that the wave functions be symmetrized.
- The ensemble of N initially inverted hydrogen atoms possesses a permutation symmetry under the exchange of any pair of atoms in the sample. This is a restricting condition that could prove difficult to satisfy in general.
- The transition between atomic levels takes place between non-degenerate levels, collisions between atoms do not affect their internal states and collisional broadening is neglected as a result of the small size of the sample (Dicke 1953).
- Although it is mentioned in Dicke (1954) that the main results of the work are independent of the type of coupling between atoms and the field, the interaction of the atoms with the radiation field in Dicke's model is assumed to be electric dipolar.
- Finally, the radiation field is assumed to be uniform through the small-sample, the electric dipoles associated to the atoms are parallel, and propagation effects neglected.

Comparing a corresponding small-sample of N neutral hydrogen atoms interacting with 21 cm line in the ISM with a Dicke sample, we can see that some of the assumptions made in the Dicke formalism hold and some do not. For example, the transitions between the hyperfine states of a hydrogen atom take place between non-degenerate levels since the external magnetic field in the ISM lifts the upper level degeneracy (see Section 3.1). Also, a small-sample of HI atoms found in many regions in the ISM would readily verify the criterion that $N \gg 1$ in a volume $\mathcal{V} < \lambda^3$, and could thus be approximately assumed to experience the same 21-cm radiation field without consideration of propagation effects. On the other hand, unlike in Dicke's sample collisional and

Doppler broadening effects should, in the most general case, be considered because, for example, collisions between hydrogen atoms affect the internal hyperfine states in their electronic ground state through spin de-excitation (Field 1958). Most importantly, it must also be noted that the type of coupling between hydrogen atoms and the 21 cm line is magnetic dipolar in nature.

Above all, the permutation symmetry of atoms, which is a key assumption in the Dicke model, is difficult to be preserved in an actual situation because of dipole-dipole interactions between the atoms. Dipole-dipole interactions have a r'^{-3} dependency and these short-range interactions become important in small-samples where the distance between atoms r' is smaller than λ (see Section 3.2 below). In the Dicke model, the symmetry breaking effect of dipole-dipole interactions is ignored. In later studies of superradiance (e.g., Gross & Haroche 1982), it has been shown that in general dipole-dipole interactions break the permutation symmetry except in those configurations where all atoms have identical close-neighbor environments. This symmetry breaking effect results in weakened correlations and a subsequent deviation from a perfectly symmetrical superradiance behavior (i.e., the $I \propto N^2$ relation in Equation [4]). In a sample of N atoms, if s atoms ($s < N$) experience a similar close-neighborhood, the correlation can build-up among this group of atoms and the intensity of radiation from the whole sample is expected to be larger than the intensity of a fully non-coherent system (I_{nc}) but smaller than that of a perfect superradiance system (I_{SR}).

In a small-sample of N neutral hydrogen atoms in the ISM it may thus appear possible to develop coherent behaviors if the permutation symmetry is conserved among a group of atoms in the sample. This is arguably a reasonable assumption on average for an ensemble of atoms within the small volumes discussed here. That is, the different atoms in the sample are likely to be subjected to the same conditions when averaged over time and space. Furthermore, we also note that in a HI-sample the magnetic dipole-dipole interactions are definitely weaker than the electric dipole-dipole interactions discussed in the literature focusing on symmetry breaking effects.

2.2. Dicke's Large-sample Model

In his first paper on superradiance, Dicke also extended his formalism to a large-sample, where the volume of the sample $\mathcal{V} > \lambda^3$ and the interatomic distance r' between some atoms can be greater than λ . He showed that in a large-sample, coherent radiation can occur in a particular direction \mathbf{k} in which the radiation from different atoms are in-phase. When the phase-matching condition is satisfied in some direction \mathbf{k} , the initial state of the system can be described by a correlated symmetric state of type (r, m_r) , and the intensity of the radiation in a solid angle along \mathbf{k} follows

$$I(\mathbf{k}) = I_0(\mathbf{k}) [(r + m)(r - m + 1)], \quad (5)$$

similar to Equation (2) for a small-sample. When a photon is emitted in the direction \mathbf{k} , the system cascades to a lower state obeying the selection rules $\Delta r = 0$, $\Delta m_r = -1$, and similar to

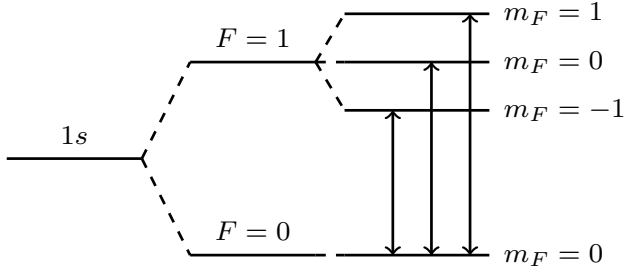


Fig. 2.— Energy level diagram for the HI 21 cm line in the presence of a Zeeman-splitting external magnetic field.

the case of a small-sample, symmetrical states of the same r are coupled to each other through coherent transitions (see Section 3.2.2). On the other hand, when a radiated photon has a wave vector $\mathbf{k}' \neq \mathbf{k}$, the states with different r (i.e., of different symmetry) can couple and consequently the coherence is weakened in the system (Dicke 1954). It follows that in a large-sample consisting of N inverted atoms, the radiation by one atom is only seen to be in-phase by a group of atoms (contrary to a small-sample where the radiation field is assumed uniform over the whole sample), and correlation can only be developed among this group. This naturally results in a radiation intensity that is greater than that of the corresponding fully non-coherent system but smaller than the superradiance intensity of a perfectly coherent system consisting of N atoms.

Finally, in a large-sample as a result of possibly large interatomic distances (i.e., $r' > \lambda$) the symmetry breaking effects of the dipole-dipole interactions are less important, whereas, the propagation effects that are absent in a small-sample cannot be neglected. The propagation of radiation over a large distance in a large-sample results in the re-absorption and re-emission of the photons and consequently leads to a non-uniform evolution of the atoms in the sample (see Section 3.3). Beyond these factors, Dicke's analysis of the large-sample includes similar assumptions as those used for the small-sample.

3. The Two-level HI-sample

Let us consider an ensemble of neutral hydrogen atoms in the electronic ground state in some region of the ISM, where it can emit or absorb photons at the $\lambda = 21$ cm wavelength. The hydrogen 21 cm line is perhaps the most important source of information in radio astronomy and arises from the transition between two levels of the hydrogen atom in the 1s ground state. The interaction between the electron spin and the proton spin in the nucleus of the atom splits the otherwise degenerate 1s energy level into the two $F = 0$ and $F = 1$ sub-levels. The $F = 1 \leftrightarrow 0$ transition in the absence of an external magnetic field produces the 21 cm line corresponding to a frequency $\nu = 1420.406$ MHz.

Considering a more realistic case, the magnetic field in a cold neutral gas is generally on the order of $10 \mu\text{G}$ (Crutcher 2012), and the energy level corresponding to $F = 1$ splits into three sub-levels identified by $m_F = -1, 0$, and 1 . The interaction between the $F = 0$ and $F = 1$ levels becomes more complicated as this splitting provides three possible hyperfine transitions, as shown in Figure 2. These hyperfine transitions link states of like parity and obey the general magnetic-dipole selection rules $\Delta F = 0, \pm 1$ and $\Delta m = 0, \pm 1$. Based on these rules, all of the three transitions shown in Figure 2 are allowed, however, depending on the relative orientation (or the polarization) of the magnetic component of the radiation field to the quantization axis of the atom, some transitions may be favored. In the more general case, there is a mixture of all three transitions with each transition exhibiting particular polarization properties. In order to better understand the coherent or cooperative evolution of a sample of N hydrogen atoms coupled to its radiation field, it will be simpler for us to focus our analysis on only one of these transitions and consider the atomic system as an ensemble of two-level atoms. Although this model represents a significant simplification, the two-level atom approximation is extensively used for, and its results well-verified in, laboratory experiments involving more complicated atomic or molecular systems with more complex energy levels (Mandel 2010).

3.1. Hamiltonian

We follow Dicke (1954) and approximate the Hamiltonian for a sample of N hydrogen atoms with each atom acting as a two-level system, while taking into account the magnetic nature of the dipole-radiation interaction applicable to this case,

$$\hat{H} = \hat{H}_0 + \hat{H}_{\text{rad}} + \hbar \sum_{j=1}^N \omega_j \left(\hat{R}_{j3} + \frac{\hat{1}}{2} \right) - \sum_{j=1}^N \hat{\mathbf{M}}_j \cdot \hat{\mathbf{B}}(\mathbf{r}_j). \quad (6)$$

In this Hamiltonian equation, \hat{H}_0 contains the translational and interatomic interaction energies of the atoms, \hat{H}_{rad} is the radiation field Hamiltonian term, $\hbar\omega_j (\hat{R}_{j3} + \hat{1}/2)$ is the internal energy of the j^{th} two-level atom ($\hat{1}$ is the unit operator), which has the eigenvalues 0 and $\hbar\omega_j$, and the last term stands for the interaction between the electromagnetic field and the magnetic dipole of the j^{th} atom $\hat{\mathbf{M}}_j$. Since this Hamiltonian is written under the magnetic dipole approximation, it implies that the magnetic field $\hat{\mathbf{B}}$ does not change considerably over the size of the atom, and is determined by its value at the position of the center of mass of the atom, \mathbf{r}_j .

As was mentioned earlier, Dicke used the correspondence between a two-level atom interacting with the radiation field and a spin-1/2 particle subjected to a static magnetic field to build his model. Accordingly he defined the operators \hat{R}_x , \hat{R}_y , \hat{R}_3 , and \hat{R}^2 in analogy to the commonly used \hat{S}_x , \hat{S}_y , \hat{S}_z , and \hat{S}^2 spin operators. Following Dicke, we write the ensuing equations

$$\hat{R}_K(\mathbf{r}) = \sum_{j=1}^N \hat{R}_{jK} \delta(\mathbf{r} - \mathbf{r}_j), \quad K = x, y, 3 \quad (7)$$

$$\hat{R}^2(\mathbf{r}) = \hat{R}_x^2 + \hat{R}_y^2 + \hat{R}_3^2 \quad (8)$$

$$[\hat{R}^2(\mathbf{r}), \hat{R}_K(\mathbf{r}')] = 0 \quad (9)$$

$$[\hat{R}_a(\mathbf{r}), \hat{R}_b(\mathbf{r}')] = i\varepsilon_{abc} \hat{R}_c(\mathbf{r}) \delta(\mathbf{r} - \mathbf{r}'), \quad a, b, c = x, y, 3, \quad (10)$$

which are similar to the relations found in the spin or general angular momentum formalisms. We can also define the raising and lowering operators

$$\hat{R}^\pm(\mathbf{r}) = \hat{R}_x(\mathbf{r}) \pm i\hat{R}_y(\mathbf{r}), \quad (11)$$

which further verify the following commutation relations

$$[\hat{R}^\pm(\mathbf{r}), \hat{R}_3(\mathbf{r}')] = \mp \hat{R}^\pm(\mathbf{r}) \delta(\mathbf{r} - \mathbf{r}') \quad (12)$$

$$[\hat{R}^+(\mathbf{r}), \hat{R}^-(\mathbf{r}')] = 2\hat{R}_3(\mathbf{r}) \delta(\mathbf{r} - \mathbf{r}'). \quad (13)$$

It is clear from the form of the Hamiltonian and the commutation relations between the operators that \hat{R}^2 and \hat{R}_3 commute with \hat{H} and, therefore, share the eigenfunctions $|r, m_r\rangle$ previously introduced to describe the state of the system.

The atomic hydrogen transitions at 21 cm are magnetic dipolar in nature and do not result from an electric dipole interaction. This brings into consideration the next leading term in our analysis, i.e., the magnetic dipole interaction found on the right-hand-side of Equation (6)

$$\hat{V}_{\text{MD}} = - \sum_{j=1}^N \hat{\mathbf{M}}_j \cdot \hat{\mathbf{B}}(\mathbf{r}_j), \quad (14)$$

which is at the center of our analysis. In general, the magnetic dipole operator $\hat{\mathbf{M}}_j$ of the j^{th} atom can be written as (Condon & Shortley 1935)

$$\hat{\mathbf{M}}_j = \mu_F \hat{\mathbf{F}}_j \quad (15)$$

$$\mu_F \simeq g_J \left[\frac{F(F+1) + J(J+1) - I(I+1)}{2F(F+1)} \right], \quad (16)$$

where $\hat{\mathbf{J}}$ is the sum of the electronic orbital $\hat{\mathbf{L}}$ and spin $\hat{\mathbf{S}}$ angular momenta (i.e., $\hat{\mathbf{J}} = \hat{\mathbf{L}} + \hat{\mathbf{S}}$), and $\hat{\mathbf{F}}$ the sum of $\hat{\mathbf{J}}$ and the nuclear spin $\hat{\mathbf{I}}$ (i.e., $\hat{\mathbf{F}} = \hat{\mathbf{J}} + \hat{\mathbf{I}}$). For the hyperfine levels of the ground

state of the hydrogen atom we have $F = 0$ and 1 , $J = S = 1/2$, $I = 1/2$, and $\mu_F \simeq g_J/2$, whereas $g_J = g_e \mu_B / \hbar$. In this equation, $g_e \simeq 2$ and μ_B is the Bohr magneton. The operator $\hat{\mathbf{F}}_j$ can also be written in terms of pseudo-spin operator $\hat{\mathbf{R}}_j$ as $\hat{\mathbf{F}}_j = \hbar \left(\hat{\mathbf{R}}_j + \hat{\mathbf{1}}/2 \right)$, allowing us to write

$$\hat{\mathbf{M}}_j = \mu_B \left(\hat{\mathbf{R}}_j + \frac{\hat{\mathbf{1}}}{2} \right). \quad (17)$$

From now on we focus our attention on the $|F = 0, m = 0\rangle \longleftrightarrow |F = 1, m = +1\rangle$ transition through which a hydrogen atom emits a left circular polarization (LCP) photon, i.e., with its electric field vector rotating counter-clockwise as seen by the observer facing the incoming wave. In general, the circular polarization state of radiation can be defined using the corresponding unit vectors \mathbf{e}_L and \mathbf{e}_R (Grynberg et al. 2010)

$$\mathbf{e}_L = -\frac{1}{\sqrt{2}} (\mathbf{e}_x + i\mathbf{e}_y) \quad (18)$$

$$\mathbf{e}_R = \frac{1}{\sqrt{2}} (\mathbf{e}_x - i\mathbf{e}_y). \quad (19)$$

Using these unit vectors and \mathbf{e}_3 to form a basis we can write the pseudo-spin operator as

$$\hat{\mathbf{R}}_j = \frac{1}{\sqrt{2}} \left(-\hat{R}_j^- \mathbf{e}_L + \hat{R}_j^+ \mathbf{e}_R \right) + \hat{R}_{j3} \mathbf{e}_3. \quad (20)$$

In a HI gas, the LCP magnetic component of the radiation propagating along the \mathbf{k} direction interacts with the magnetic dipole of a hydrogen atom resulting in a transition between the two hyperfine levels. The corresponding magnetic field operator can be expressed as

$$\hat{\mathbf{B}}_L(\mathbf{r}, t) = \sum_{\mathbf{k}} \left[\hat{B}_{L\mathbf{k}}^+(\mathbf{r}) e^{-i\omega_k t} \mathbf{e}_L + \hat{B}_{L\mathbf{k}}^-(\mathbf{r}) e^{i\omega_k t} \mathbf{e}_L^* \right], \quad (21)$$

where

$$\hat{B}_{L\mathbf{k}}^+(\mathbf{r}) = \frac{1}{c} \sqrt{\frac{\hbar\omega_k}{2\epsilon_0 V}} \hat{a}_{L\mathbf{k}} e^{i\mathbf{k}\cdot\mathbf{r}} \quad (22)$$

$$= \left(\hat{B}_{L\mathbf{k}}^- \right)^\dagger, \quad (23)$$

and V is the arbitrary volume of quantization. In Equation (22), $a_{L\mathbf{k}}$ and $a_{L\mathbf{k}}^\dagger$ are, respectively, the second quantization field annihilation and creation operators, and obey the following commutation relation

$$[\hat{a}_{L\mathbf{k}}, \hat{a}_{L\mathbf{k}'}^\dagger] = \hat{1}\delta_{\mathbf{k}\mathbf{k}'}.$$
 (24)

As a result, one can express the magnetic dipole interaction term in Equation (14) for transitions involving only LCP photons as

$$\hat{V}_{\text{MD}} = -\mu_B \sum_{j=1}^N \hat{\mathbf{R}}_j \cdot \hat{\mathbf{B}}_L(\mathbf{r}_j)$$
 (25)

$$= \frac{\mu_B}{\sqrt{2}c} \sum_{j=1}^N \sum_{\mathbf{k}} \sqrt{\frac{\hbar\omega_k}{2\epsilon_0 V}} \left(\hat{R}_j^+ \hat{a}_{L\mathbf{k}} e^{i\mathbf{k}\cdot\mathbf{r}_j} + \hat{R}_j^- \hat{a}_{L\mathbf{k}}^\dagger e^{-i\mathbf{k}\cdot\mathbf{r}_j} \right),$$
 (26)

using $\hat{\mathbf{R}} \cdot \mathbf{e}_L = -\hat{R}^+/\sqrt{2}$ and $\hat{\mathbf{R}} \cdot \mathbf{e}_L^* = -\hat{R}^-/\sqrt{2}$. It will also prove useful to write Equation (26) in the following form

$$\hat{V}_{\text{MD}} = - \int_V \hat{\mathcal{M}}(\mathbf{r}) \cdot \hat{\mathbf{B}}_L(\mathbf{r}) d^3r,$$
 (27)

which allows a definition of the transverse macroscopic magnetization operator $\hat{\mathcal{M}}(\mathbf{r})$ in terms of the raising and lowering density operators \hat{R}^+ and \hat{R}^- as follows

$$\hat{\mathcal{M}}(\mathbf{r}) = -\frac{\mu_B}{\sqrt{2}} \left[\hat{R}^-(\mathbf{r}) \mathbf{e}_L + \hat{R}^+(\mathbf{r}) \mathbf{e}_L^* \right]$$
 (28)

$$\equiv \hat{\mathcal{M}}^+(\mathbf{r}) + \hat{\mathcal{M}}^-(\mathbf{r}).$$
 (29)

We note that the H_0 term in the Dicke Hamiltonian of Equation (6) includes the Coulomb interaction between atoms in a Dicke sample, which can generally be approximated by the electrostatic interaction between electric-dipole moments of the atoms in a sample. Since the Coulomb interaction term is much smaller than the non-interacting Hamiltonian of individual atoms, it can be evaluated using perturbation theory. In a sample of hydrogen atoms with all atoms in the 1s state the first-order energy correction due to the electrostatic dipole-dipole interaction vanishes because of the symmetry of this state. It can be shown that the second-order energy correction of the electrostatic dipole-dipole interaction between two hydrogen atoms in the 1s state is proportional to r'^{-6} , where r' is the interatomic distance (the r'^{-6} interaction energy is called London dispersion energy, which is a type of Van der Waals interaction energy; see Cohen-Tannoudji et al. 1977). If one includes the spin of the electrons, then the magnetic dipole-dipole interaction between the electron spin of different hydrogen atoms must also be considered and a correction term proportional to α^2/r'^3 must be added to the interaction energy relation, with $\alpha \simeq 1/137$ the fine-structure constant (Meath 2004). The magnetic dipole-dipole interactions may be particularly important in the study

of matter-radiation interaction in a HI gas as they not only modify the interaction energy but also affect the transition rates between energy levels of the hydrogen atoms in a sample (see Section 3.2 below).

Finally, we note that in our modified Dicke Hamiltonian for a HI-sample, the effects of the hyperfine interaction between the proton and electron spins within a single hydrogen atom and the Zeeman interaction due to an external magnetic field would be included in the frequency ω_j of the atomic transition.

3.2. Magnetic Dipole-dipole Interaction Between Hydrogen Atoms

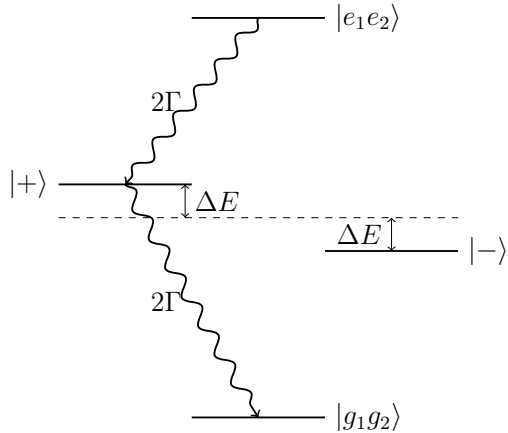


Fig. 3.— The two-hydrogen-atom system. When $kr' \ll 1$ the upper and lower symmetric states $|e_1e_2\rangle$ and $|g_1g_2\rangle$, respectively, couple to the intermediate symmetric state $|+\rangle$ at the enhanced transition rate 2Γ , where Γ is the transition rate of a single atom acting independently. In contrast, the antisymmetric state $|-\rangle$ cannot couple to the upper and lower states because of the cooperative behavior between the two atoms. The energy level shifts $\pm\Delta E$ for the $|\pm\rangle$ states are also shown.

3.2.1. Hydrogen Atoms Separated by a Small interatomic Distance ($r' < \lambda$)

In order to have a better understanding of how cooperative behavior is built up in a sample of N atoms, it is helpful to first study the simpler case of two atoms. We specifically consider a system consisting of two hydrogen atoms, once again assuming each atom is a two-level system with the excited state $|e\rangle$ ($F = 1$) and the ground state $|g\rangle$ ($F = 0$). The two atoms are initially excited and the state of the system is given by $|e_1\rangle \otimes |e_2\rangle = |e_1e_2\rangle$. Eventually one of the two atoms spontaneously decays to its ground state emitting a photon with a wavelength λ and energy $\hbar\omega$. If the interatomic distance r' is much smaller than λ (i.e., $kr' \ll 1$) and the two atoms are

identical, then one cannot say which atom has emitted the photon nor which is in a given state. In the case of the two-level hydrogen atom discussed here, this decay rate must be related to that of the corresponding magnetic dipole transition given by (MKS units)

$$\Gamma = \frac{\mu_0 k^3 |\langle e | \hat{\mathbf{M}} | g \rangle|^2}{3 \hbar \pi}. \quad (30)$$

We can furthermore express the state of the system by either a symmetric $|+\rangle$ or antisymmetric $|-\rangle$ combination of the $|e_1 g_2\rangle$ and $|g_1 e_2\rangle$ state vectors such as

$$|+\rangle = \frac{1}{\sqrt{2}} (|e_1 g_2\rangle + |g_1 e_2\rangle) \quad (31)$$

$$|-\rangle = \frac{1}{\sqrt{2}} (|e_1 g_2\rangle - |g_1 e_2\rangle), \quad (32)$$

which, at this stage of our analysis, have the same energy and are thus degenerate (see below).

We now refine this model by adding the magnetic dipole-dipole interaction term to the system's Hamiltonian. In this model the magnetic dipole from one atom, say, $\hat{\mathbf{M}}_1$, interacts with the magnetic field $\hat{\mathbf{B}}_2$ due to the dipole of the other atom located at a position \mathbf{r}' away in the near-field, where $kr' \ll 1$ (Jackson 1999)

$$\hat{\mathbf{B}}_2(\mathbf{r}') = \frac{\mu_0}{4\pi} \left[\frac{\cos(kr')}{r'^3} + \frac{\sin(kr')}{r'^2} \right] \left[3\mathbf{e}_{r'} (\mathbf{e}_{r'} \cdot \hat{\mathbf{M}}_2) - \hat{\mathbf{M}}_2 \right]. \quad (33)$$

It can be shown that when the two dipoles are aligned, the term of the interaction Hamiltonian that is relevant to the present discussion is

$$\hat{H}_{dd} = -\frac{\mu_0 k^3 \mu_B^2}{2\pi} (3|\beta|^2 - 1) \left[\frac{\cos(kr')}{(kr')^3} + \frac{\sin(kr')}{(kr')^2} \right] (\hat{R}_1^+ \hat{R}_2^- + \hat{R}_1^- \hat{R}_2^+), \quad (34)$$

with $\beta = \mathbf{e}_L \cdot \mathbf{e}_{r'}$. It can further be shown, through a simple diagonalization exercise, that this interaction Hamiltonian lifts the degeneracy between the $|+\rangle$ and $|-\rangle$ states of Equations (31) and (32), with their corresponding energies becoming (Protsenko 2006)

$$E_{\pm} = E_0 \pm \Delta E, \quad (35)$$

with E_0 the unperturbed energy of the states and

$$\Delta E = \frac{\mu_0 k^3 \mu_B^2}{2\pi} (3|\beta|^2 - 1) \left[\frac{\cos(kr')}{(kr')^3} + \frac{\sin(kr')}{(kr')^2} \right]. \quad (36)$$

It is then also possible to verify through Equation (30), setting $\hat{\mathbf{M}} = \hat{\mathbf{M}}_1 + \hat{\mathbf{M}}_2$, that the transition rates Γ_{\pm} for the $|\pm\rangle$ states with the initial $|e_1e_2\rangle$ and final $|g_1g_2\rangle$ states are

$$\Gamma_+ = 2\Gamma \quad (37)$$

$$\Gamma_- = 0, \quad (38)$$

where Γ is the transition rate of a single atom acting independently.

The differentiation of energy levels brought about by the magnetic dipole-dipole interaction is, therefore, seen to be a function of β and the interatomic distance r' . More important, however, is the doubling of the transition rate for the symmetric state $|+\rangle$, and the cancellation of that of the antisymmetric state $|-\rangle$. Such enhanced and reduced rates are respectively associated to superradiance and subradiance. This scenario for the two-atom system is depicted in Figure 3.

This behavior can also be understood by considering the symmetry of the system's Hamiltonian and states. The fact that, as could easily be verified, the Hamiltonian of the system of two atoms (including the magnetic dipole term V_{MD}) is totally symmetric under the permutation of the two aligned atoms when $kr' \ll 1$ implies that only states of like symmetry can be coupled. It follows that since the initial state $|e_1e_2\rangle$ of the fully inverted system is also symmetric, it can only couple to the $|+\rangle$ intermediate state, and from there to the symmetric ground state of the system $|g_1g_2\rangle$. Accordingly, it is interesting to note that under these conditions a system prepared in the intermediate antisymmetric state $|-\rangle$ will not decay to the ground state since $\Gamma_- = 0$. This is evidently different from the case of a non-coherent system where the both atoms eventually decay to their individual ground state $|g\rangle$ at the rate Γ . We therefore see that superradiance and subradiance are characteristics of a coherent system, where the intensity of radiation does not scale linearly with the number of atoms, as is the case for a non-coherent system.

When the effect discussed here is generalized to a sample composed of N atoms confined within a volume $\mathcal{V} \ll \lambda^3$ (a small-sample), we find that some of the conditions that prevailed for the two-atom case are not realized. Most importantly, Equations (36) and (35) indicate that this interaction leads to a distribution of energy levels in the system unless the atoms all have similar nearest neighborhood (e.g., a ring-like periodic distribution of atoms; Gross & Haroche 1982). This spread in energy levels will tend to reduce the strength of the superradiance effect.

It has nonetheless been observed through numerical calculations and experiments that coherent behaviors still apply to N -atom small-sample systems where radiation is of long enough wavelength (Gross et al. 1979), as is the case for 21 cm line. For $kr' \sim 1$ the ratio $\Delta E/E_0 \sim \Gamma/\omega$ is exceedingly small for the 21 cm line, and the time-scale associated with the energy shifts is on the order of $\hbar/\Delta E \sim (kr')^3 \Gamma^{-1}$ (Benedict et. al. 1996), which for the HI densities considered in this paper renders this type of dephasing negligible. As will be discussed later, dephasing due to collisions are more likely to set the time-scale for homogeneous dephasing. The same is not necessarily true at short wavelengths where it is very difficult to place a large number of atoms within a sub-wavelength

dimension in a regular pattern, and in such a sample strong dipole-dipole interactions break the symmetry and terminate the coherent behavior by introducing large energy-level shifts. Thus most of the experimental observations of superradiance took place at longer wavelengths (i.e., in the infrared as opposed to optical; Benedict et. al. 1996).

For an inverted N -atom small-sample with initially uncorrelated dipoles the first photon emitted by one of the atoms interacts with the dipole moments of the other atoms, resulting in the build up of correlation between them. After some time, known as the delay time t_D , a very high degree of correlation is developed in the system, where in the strongest superradiance regime, the N microscopic dipoles eventually act like one macroscopic dipole. The rate of emission is then enhanced to NT , while the radiation intensity is proportional to N^2 and becomes highly directional, being focussed in a beam with a temporal half-width on the order of $1/(NT)$.

It should also be noted that the correlation between dipoles can be triggered by an external source such as an input radiation field. This can happen if the input radiation field is stronger than the spontaneous fluctuations in the sample, and the coupling of the dipoles to the external field leads to coherent behaviors. An enhancement of radiation through coupling to an external field is called *triggered superradiance* (Benedict et. al. 1996).

It can be shown that the superradiance radiation intensity I_{SR} of an ideal HI small-sample composed of N inverted atoms is given by (Dicke 1954; Gross & Haroche 1982; Benedict et. al. 1996)

$$I_{SR} = N^2 \hbar \omega \Gamma \cosh^{-2} [NT(t - t_D)], \quad (39)$$

where $\hbar \omega$ is the energy of the corresponding atomic transition and the aforementioned delay time $t_D = (NT)^{-1} \ln(N)$. In Figure 4 the radiation intensity of a HI small-sample with $N = 75$ atoms confined within a cube of length 4 cm ($\simeq \lambda/5$ for the 21 cm line) is plotted as a function of time using Equation (39). The intensity is normalized to NI_{nc} , where $I_{nc} = N\hbar\omega\Gamma$ is for the corresponding non-coherent small-sample. It can be seen in Figure 4 that the energy stored in the small-sample is radiated away in a single burst. After time $t = t_D$, the intensity reaches its maximum value, N times that of the non-coherent intensity, and the peak intensity of the normalized plot becomes equal to one. In this HI sample, $\Gamma^{-1} = 3.5 \times 10^{14}$ sec (Draine 2011), the delay time $t_D = 2.0 \times 10^{13}$ sec, and the characteristic time of superradiance is $T_R = (NT)^{-1} = 4.6 \times 10^{12}$ sec. It should also be pointed out that in such a sample the correlation between dipoles is initiated by internal spontaneous fluctuations and it is assumed that we are dealing with an ideal system, where the dipole-dipole symmetry breaking effects are negligible and there is no other relaxation mechanism (i.e., cooperative emission is the only decay mechanism).

In a real system, there are some relaxation and dephasing effects that compete with the build-up of the correlation, and in order to subsequently have superradiance, its characteristics time-scale T_R and delay time t_D must be shorter than (in some exceptional cases on the order of) the

relaxation/dephasing time-scales (Gross & Haroche 1982; Benedict et. al. 1996). The non-ideal case will be discussed in Section 3.3.1.

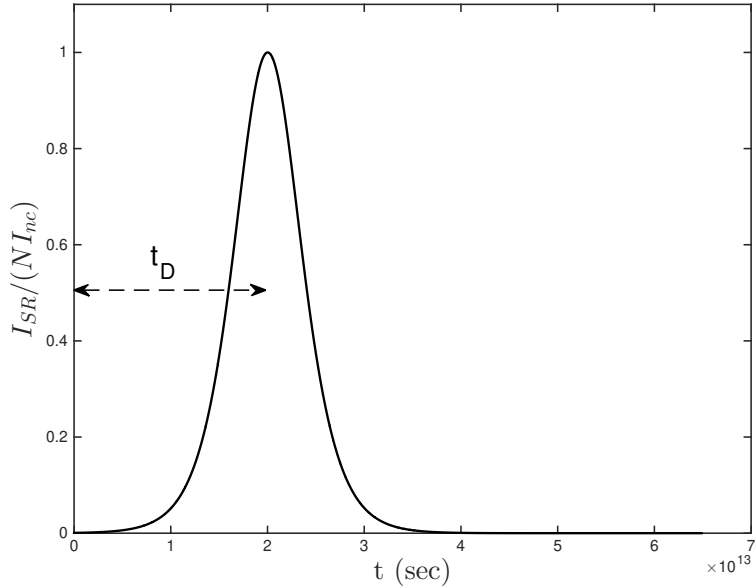


Fig. 4.— The ideal HI small-sample superradiant system. The radiation intensity is plotted as a function of time t , for $N = 75$ atoms confined within a cube of $L = 4$ cm. After the delay time $t_D = 2.0 \times 10^{13}$ seconds the system radiates coherently in a single burst of radiation.

3.2.2. Two Hydrogen Atoms Separated by a Larger interatomic Distance ($r' > \lambda$)

In the previous section we discussed the case of two two-level hydrogen atoms when the interatomic distance r' is small compared to the wavelength λ . It was then mentioned that for such small interatomic distances the atoms are indistinguishable and the intermediate states of the system can be expressed by the symmetric $|+\rangle$ or the antisymmetric $|-\rangle$ states. It was also emphasized that these states never couple with each other as a result of the interaction with the radiation field when their dipoles are aligned and $kr' \ll 1$. These considerations have to be modified when we consider larger interatomic distances (i.e., $r' > \lambda$).

Let us assume that the atoms are prepared initially in their excited states, with the state of the two-atom system given by $|e_1 e_2\rangle$. Similar to the sub-wavelength case, a first photon is radiated leaving the system in an intermediate state, which unlike as we did for the sub-wavelength case, will be described with any combination of $|e_1 g_2\rangle$ and $|g_1 e_2\rangle$ states with each having equal probability contributions, i.e., not only by the $|+\rangle$ and $|-\rangle$ states. More precisely, if we associate the general symmetric state

$$|S\rangle = \frac{1}{\sqrt{2}} (|e_1g_2\rangle + e^{i\phi}|g_1e_2\rangle) \quad (40)$$

to the intermediate state shown in the left side of Figure 5, then we should assign its orthogonal antisymmetric state

$$|A\rangle = \frac{1}{\sqrt{2}} (|e_1g_2\rangle - e^{i\phi}|g_1e_2\rangle) \quad (41)$$

to the intermediate state on the right side of the figure (Dicke 1964). In Equations (40) and (41), ϕ is a phase term discriminating between the multiple choices for the intermediate states. To get a better understanding of the transition probabilities for these states, it is useful to refer back to Equation (26) for the magnetic dipole interaction term with a radiation field for two atoms separated by \mathbf{r}' and for a given \mathbf{k} . We then find that for coupling to, say, the $|e_1e_2\rangle$ state the following term comes into play

$$\hat{V}_{\text{MD}} \propto \hat{R}_1^+ + \hat{R}_2^+ e^{ikr' \cos(\theta')}, \quad (42)$$

where θ' is the angle between \mathbf{k} and \mathbf{r}' . Given that the transition probability (and rates) are proportional to $|\langle e_1e_2 | \hat{V}_{\text{MD}} | S \rangle|^2$ and $|\langle e_1e_2 | \hat{V}_{\text{MD}} | A \rangle|^2$ (Grynberg et al. 2010), we calculate using Equation (40), (41), and (42)

$$\Gamma_S \propto \cos^2 \left\{ \frac{1}{2} [\phi - kr' \cos(\theta')] \right\} \quad (43)$$

$$\Gamma_A \propto \sin^2 \left\{ \frac{1}{2} [\phi - kr' \cos(\theta')] \right\}. \quad (44)$$

We therefore see that, although the first photon can be emitted in any direction θ' , its direction of emission determines ϕ and the intermediate state of the system since the transition probabilities peak at $\phi - kr' \cos(\theta') = 2m\pi$ for Γ_S and $\phi - kr' \cos(\theta') = n\pi$ for Γ_A (m and $n \neq 0$ are integers). Going through the same exercise for the $|g_1g_2\rangle$ state shows a similar dependency on θ' and ϕ as in Equations (43) and (44), which implies that these transitions rates will also be likely to peak at the same value of ϕ . It follows that there is an angular correlation between two successive photons, where the direction of the second photon is correlated with the direction of the first. This angular correlation can take place even when the atoms are placed several wavelengths apart, as a result of their coupling to a common electromagnetic field, and favors intense radiation along elongated geometries (e.g., pencil-like or cylindrical structures; Dicke 1964).

Depending on the intermediate state of the system two different classes of transitions are possible; coherent and non-coherent. If the emission of the first photon leaves the system in a

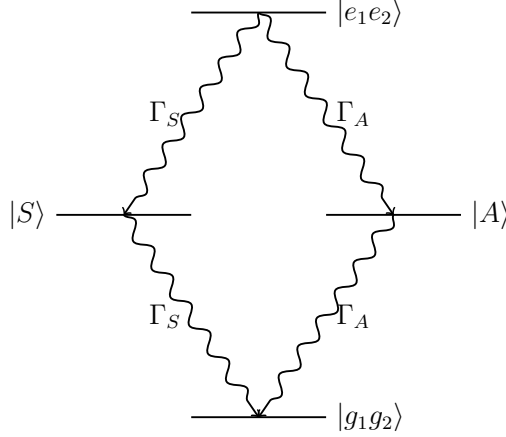


Fig. 5.— The two-hydrogen-atom system with $r' > \lambda$. The upper and lower symmetric states $|e_1e_2\rangle$ and $|g_1g_2\rangle$, respectively, couple to the intermediate symmetric $|S\rangle$ and antisymmetric $|A\rangle$ states with the corresponding transition rates Γ_S and Γ_A . The direction of emission of the first photon determines the intermediate state of the system, and the direction of the second photon is correlated with that of the first.

symmetric intermediate state (e.g., $|S\rangle$) the symmetric coupling to the radiation field results in the coherent behavior and consequently the system decays to the symmetric ground state $|g_1g_2\rangle$ with the corresponding transition rate shown in Figure 5. On the other hand, if the system is in the antisymmetric intermediate state $|A\rangle$ the coupling to the radiation field will be antisymmetric under the exchange of the atoms as they interact with the non-uniform electromagnetic field, and the system decays non-coherently to the ground state $|g_1g_2\rangle$ with the decay rate Γ_A .

We can also explain this classically by considering two classical radiators separated by a distance $r' > \lambda$. Over large distances, the phase and the polarization of the radiation field emitted by each radiator varies from place to place. When the radiation from the two identical radiators interfere constructively, the intensity of the total field is given by

$$I_{\text{tot}} \propto \langle (\mathbf{B}_1 + \mathbf{B}_2)^2 \rangle \quad (45)$$

$$\propto \langle B_1^2 \rangle + \langle B_2^2 \rangle + 2 \langle \mathbf{B}_1 \cdot \mathbf{B}_2 \rangle, \quad (46)$$

and can become as large as four times of the intensity of a single radiator I_0 if

$$\langle \mathbf{B}_1 \cdot \mathbf{B}_2 \rangle \propto I_0. \quad (47)$$

If the phase of the radiation from different radiators does not match perfectly, the term containing the correlation $\langle \mathbf{B}_1 \cdot \mathbf{B}_2 \rangle$ in Equation (46) becomes smaller than I_0 and consequently the total

intensity I_{tot} decreases until it reaches its minimum for completely out of phase radiators. Furthermore, the correlation term can vanish when radiators act independently. In this case, the total intensity becomes equal to the sum of the intensities of the two independent radiators (the so-called non-coherent system).

3.3. The N -atom Large-sample ($\mathcal{V} > \lambda^3$)

We can extend our discussion for the case of two distant atoms (i.e., $r' > \lambda$) to a large-sample consisting of N atoms distributed over a volume $\mathcal{V} > \lambda^3$. As stated above, the build-up of correlations in an extended N -atom sample can be understood as a constructive interference of the radiation by different atoms. In a large-sample as a result of propagation over large distances (i.e., larger than λ) the phase of the radiation varies throughout the sample ($kr' \gg 1$ and $e^{i\mathbf{k}\cdot\mathbf{r}'} \approx 1$). Consequently, the phase of the atomic magnetization differs with position. In an inverted large-sample, the radiation from different atoms interfere with each other, and when the magnetization of the radiators are perfectly in phase, an intense propagating wave is produced in one direction (the phase-matching condition cannot be satisfied in all directions).

In order to better understand the phase-matching process, it is useful to go back to the angular correlation effect described in the two-atom case. In a large-sample of N inverted atoms, when the first photon is emitted other atoms interact with its radiation field and the direction of the next photon is affected by the first one. In a more general sense, when a photon is radiated in a particular direction \mathbf{k} , it becomes more probable to observe the second photon in the same direction \mathbf{k} than any other direction. Thus, as the atoms radiate, an angular correlation builds up in the sample that triggers the phase-matching process in a well-defined direction.

Ideal superradiance is the result of the symmetrical evolution of an atom-field system, and in a large-sample, the propagation effects result in the non-uniform evolution of the atoms in the sample. In order to better understand propagation effects in a large-sample, the atomic medium can be divided into small identical slices with dimensions larger than λ but much smaller than the length of the sample. A microscopic dipole is then associated to each slice with its magnitude being proportional to the number of excited atoms in the corresponding slice. At the beginning, the dipoles in different slices are independent and their radiation uncorrelated. After some time (or the so-called retarded-time delay τ_D ; see Equation (58) below), as they interact with their common radiation field, the dipoles lock to a common phase, and act as a single macroscopic dipole radiating intensely with $I_{\text{SR}} = NfI_{\text{nc}}$, where Nf is the enhancement factor of the superradiant intensity I_{SR} over the non-coherent intensity I_{nc} determined by the efficiency of the common phase-locking process (through the value of $f \leq 1$). The enhancement factor Nf can become very large in samples with $N \gg 1$, and it converges to N in an atomic system with dimensions of the order of λ resulting in $I_{\text{SR}} = NI_{\text{nc}}$ for the most efficient phase-locking process seen in a small-sample. In other words, $f < 1$ implies a limited coherent behavior in a large-sample resulting in a smaller output intensity and weakened superradiance, whereas $f = 1$ indicates a fully coherent behavior leading to an intense

radiation and perfect superradiance (Gross & Haroche 1982; MacGillivray & Feld 1976).

This approach has the shortcoming that it cannot explain the initiation of the radiation in the system by spontaneous fluctuations, and to overcome this problem phenomenological fluctuations of dipoles in the initial stages of the evolution can be added to the formalism. In contrast, triggered superradiance can be fully explained in this manner as the correlation process is initiated by an external field, which can be defined classically. It must be pointed out that the results of this method are valid only if the propagation time of the radiation τ_E through a sample of length L (i.e., $\tau_E = L/c$) is smaller than the superradiance characteristic time T_R given by

$$T_R = \tau_{sp} \frac{16\pi}{3n\lambda^2 L}, \quad (48)$$

where $\tau_{sp} = 1/\Gamma$ is the spontaneous decay time of a single atom and n the density of inverted atoms (MacGillivray & Feld 1976; Rosenberg & DeTemple 1981). This condition (i.e., $\tau_E < T_R$) is known as Arecchi-Courtens condition, and it ensures that the atomic magnetization in different parts of the sample can lock into a common phase and coherent behavior can develop through the sample.

In Appendix A, we derive the evolution equations for the radiation field and the atomic system using the Heisenberg representation, while in Appendix B we solve the corresponding Maxwell-Bloch system of equations, at resonance, within the framework of the slowly varying envelope approximation (SVEA). To do so, we adopted the following form for the radiation magnetic field and atomic magnetization

$$\hat{B}_L^\pm(\mathbf{r}, t) = \hat{B}_0^\pm(\mathbf{r}, t) e^{\pm i(kz - \omega t)} \quad (49)$$

$$\hat{\mathcal{M}}^\pm(\mathbf{r}, t) = \hat{\mathcal{M}}_0^\pm(\mathbf{r}, t) e^{\pm i(kz - \omega t)}, \quad (50)$$

with \hat{B}_0^\pm and $\hat{\mathcal{M}}_0^\pm$ corresponding slow varying envelope operators. The superradiance of a cylindrical large-sample of length L under ideal conditions is then found to be determined by the following equations for, respectively, the magnetization, the population inversion, and the magnetic field

$$\hat{\mathcal{M}}_0^+ = \frac{\mu_B N}{2\sqrt{2}V} \sin(\theta) \quad (51)$$

$$\hat{\mathbb{N}} = \frac{N}{V} \cos(\theta) \quad (52)$$

$$\hat{B}_0^+ = \frac{i\mu_B}{2\sqrt{2}\gamma} \frac{\partial\theta}{\partial\tau}, \quad (53)$$

where $\gamma = \mu_B^2/2\hbar$. The solution for the Bloch angle θ as a function of the retarded-time $\tau = t - L/c$ is obtained through the so-called Sine-Gordon equation

$$\frac{d^2\theta}{dq^2} + \frac{1}{q} \frac{d\theta}{dq} = \sin(\theta) \quad (54)$$

with

$$q = 2\sqrt{\frac{z\tau}{LT_R}}. \quad (55)$$

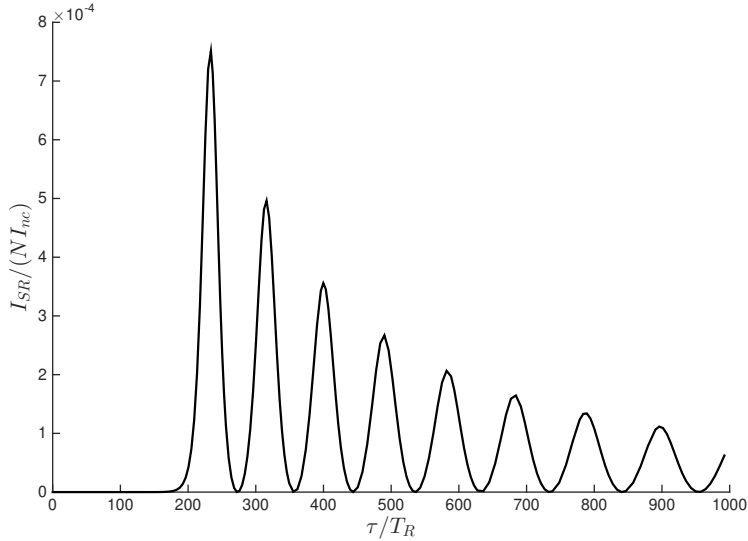


Fig. 6.— The ideal cylindrical HI large-sample. The radiation intensity, scaled to NI_{nc} , is plotted versus the retarded time $\tau = t - L/c$ normalized to the superradiance characteristic time-scale T_R . The length and radius of the cylinder are, respectively, $L = 0.02 cT_R$ and $w = 0.036 (cT_R)^{1/2}$.

In Figure 6 we show the solution for the radiation intensity of such an ideal cylindrical large-sample of HI atoms of length $L = 0.02 cT_R$, where c is the speed of the light, by numerically solving Equations (51) to (55). For these calculations we set a Fresnel number of unity to reduce the impact of diffraction losses, which are not taken into account in our model. This yields a cylinder of radius

$$w = \sqrt{\frac{\lambda L}{\pi}}, \quad (56)$$

which for our ideal sample results in $w = 0.036 (cT_R)^{1/2}$.

In this sample, the Arecchi-Courtens condition is satisfied (i.e., $\tau_E \ll T_R$) allowing the use of the homogeneous condition $\theta_0 = 4.9 \times 10^{-12}$ rad for the initial value of the Bloch angle. More precisely, for the large-sample used for the figure we assumed that internal fluctuations dominate

over triggered superradiance, and the initial Bloch angle was set with $\theta_0 = 2/\sqrt{N}$ (Gross & Haroche 1982).

In Figure 6, the retarded-time axis is scaled to T_R and the radiation intensity to NI_{nc} , i.e., the number of inverted atom times the corresponding non-coherent intensity that would otherwise be expected from such a sample. More precisely, for comparison purposes we consider the non-coherent intensity emanating through the sample's end-fire of area A , within the superradiance radiation beam solid-angle $\phi_D = \lambda^2/A$ (in the direction \mathbf{k} along which the phase-locking condition is satisfied) normalized to the solid angle associated to the total non-coherent radiation. We thus have

$$\begin{aligned} I_{nc} &= N\hbar\omega \left(\frac{1}{A\tau_{sp}} \right) \left(\frac{\phi_D}{4\pi} \right) \\ &= \frac{4}{3} \frac{\hbar\omega}{AT_R}, \end{aligned} \quad (57)$$

where Equation (48) was used for the last step and $N\hbar\omega$ is the total energy initially stored in the sample. As shown in the figure, this energy is radiated away through multiple bursts, a phenomenon known as ringing effect. This effect can be explained by the fact that different atoms in different locations in the sample radiate at different times. In other words, an atom at location $z = z_0$, prepared in the excited state at $\tau = 0$, radiates its energy away and decays to its ground state, then later on absorbs the energy radiated by another atom at a location $z < z_0$ and becomes excited leading to another radiation event.

In a large-sample, just as in a small-sample, internal field fluctuations or an external field trigger superradiance, and after the delay time τ_D the atoms radiate coherently. But contrary to a small-sample, the large-sample delay time depends on the initial conditions and is given by (Benedict et. al. 1996)

$$\tau_D \simeq \frac{T_R}{4} \left| \ln \left(\frac{\theta_0}{2\pi} \right) \right|^2. \quad (58)$$

In Figure 6 the first burst of radiation occurs after $\tau_D \simeq 160 T_R$, which is consistent with the value one finds using Equation (58). As can also be seen, this first intensity burst only carries out a fraction of the total energy stored in the sample, while the remaining radiation happens through subsequent bursts. The number of burst events depends on the length of the sample, and as the length is increased radiation emanates through a larger number of bursts, while the peak intensity of consecutive burst events gradually drops. This is a consequence of energy conservation and the fact that in a larger (i.e., longer) sample radiation from different groups of atoms along the sample arrive at the end-fire at different times, and the process of absorbing the radiation, developing correlations between the dipoles, and eventually re-emitting the radiation repeats multiple times over a very

long period of time. On the other hand, when the length of the sample is decreased the ringing effect becomes weaker until, for a small-sample of dimension of order of λ , it totally washes out and we only observe a single burst of radiation carrying away all the energy stored in the system (as in Figure 4). Finally, we note that although the maximum radiation intensity seen in Figure 6 seem to imply that $f \sim 0.001 \ll 1$, the large number of atoms present in the sample ensures that $I_{\text{SR}} \gg I_{\text{nc}}$ (see Section 4). We should also note, however, that the Sine-Gordon equation is very sensitive to initial conditions. It therefore follows that the exact shape of the intensity curve, e.g., the number of bursts in Figure 6, is also strongly dependent on θ_0 .

3.3.1. Non-ideal Case – Dephasing Effects

As was mentioned earlier, the characteristics time-scale of superradiance T_R and the delay time τ_D (for a large-sample) must be shorter than the relaxation/dephasing time-scales to allow the build-up of correlations in a non-ideal sample. These effects include natural broadening due to the spontaneous decay time-scale τ_{sp} of a single atom and collisional broadening related to the mean time between collisions τ_{coll} for an atom in the sample. Although, as was stated in Section 1, our analysis is aimed at regions of the ISM where thermal equilibrium has not been reached and where consequently the assignation of a temperature to determine, for example, collision rates is perhaps ill-defined, we will nonetheless adopt such a procedure for the rest of our discussion to get a sense of the time-scales involved. Accordingly, in a HI gas different types of collisions can take place depending on the temperature and density. For environments of temperatures ranging from approximately 10 K to 300 K, which are the focus of our analysis, collisions between two neutral hydrogen atoms (H-H collisions) dominate and fall into two categories: elastic and inelastic. During an elastic H-H collision, the spacing between the atomic energy levels are slightly affected but no transition between them is induced. The change in energy spacing occurs as a result of short-range interaction forces between the two colliding particles and induces a phase shift in the wave function of the scattered atoms. After a number of elastic collisions, an atom can lose coherence with the interacting radiation field as a result of the randomness in the perturbations. On the other hand, in an inelastic H-H collision the internal energy of the hydrogen atoms will be changed. This occurs when the two hydrogen atoms with oppositely directed electron spins approach each other at distances less than approximately 10^{-8} cm. This process is known as electron exchange or spin de-excitation effect. As a result of such a collision the induced phase shift can lead to a change in the internal spin states (Wittke et al. 1956), and it is found that spin de-excitation is the dominating relaxation process in a high density collision-dominated HI gas. We therefore find that H-H collisions not only can affect the strength of a potential coherent 21-cm radiation by removing from the population of the excited hyperfine states, they also contribute to the line breadth and can change the shape of the spectral line by affecting the spacing between internal energy levels. For example, the time-scale of H-H collisions are estimated to be on the order of 10^8 sec in the case of elastic scattering and 10^9 sec for spin de-excitations, using the mean effective collisional cross sections given in Irwin (2007) for a HI gas at $T = 100$ K and $n = 10 \text{ cm}^{-3}$. The mean time between

collision τ_{coll} is thus set to the shortest of these time-scales and must at least be larger than T_R and τ_D to allow coherent behavior (see Section 4).

In addition, other broadening effects, such as Doppler broadening, are further dephasing mechanisms that can destroy cooperative behavior if their time-scales (importantly the so-called Doppler dephasing time, i.e., the reciprocal of the Doppler width) are smaller than T_R and τ_D (Meziane et al. 2002; Bonifacio & Lugiato 1975). In a thermally relaxed gas, thermal motions are probably the most important dephasing effects and result in line broadenings that correspond to very short dephasing time-scales (e.g., $T_{\text{therm}} \sim 10^{-3}$ sec at $T = 100$ K). In the presence of such strong dephasing effects, correlations cannot develop between the dipoles and any coherent interaction will be terminated right from the start. Hence our earlier comment that we do not expect to find superradiance under conditions of thermal equilibrium, but potentially only in (out-of-equilibrium) regions where strong velocity coherence can be maintained along the line-of-sight. Furthermore, this condition may be only met among a group of atoms in such regions, therefore reducing the number of inverted atoms in the sample that could participate in coherent interactions. However, we know from maser observations that a high level of velocity coherence can be achieved in some regions of the ISM, and we expect that superradiance could only happen under similar conditions. As was mentioned in Section 1, the main inversion pumping mechanism likely involved for the 21 cm transition points to the surroundings of HII as potentials sites for superradiance in this spectral line. It follows that we should also anticipate analogous (i.e., very small) volume filling factor for the emitting regions of superradiant sources as for masers.

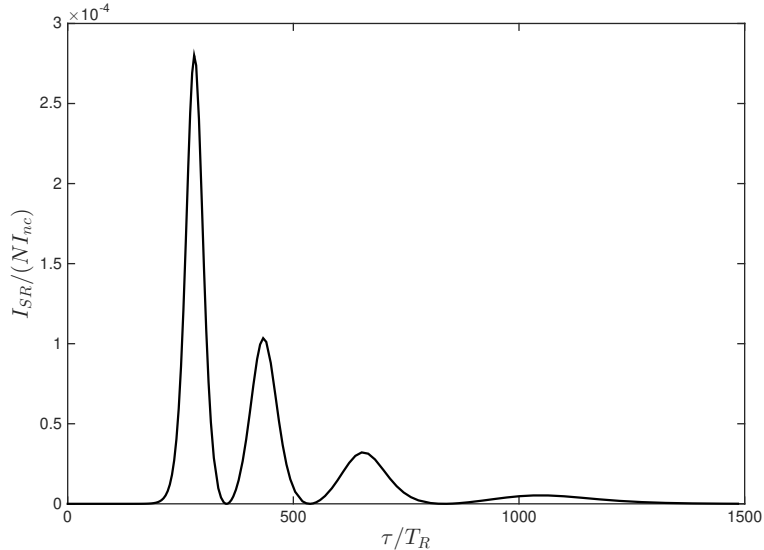


Fig. 7.— The non-ideal HI cylindrical large-sample. All parameters are as in Figure 6, except that dephasing/relaxation effects are included for the special case where they are characterized by a single time-scale $T' = 541 T_R$. The ringing effect is weakened as a result of the dephasing.

In Figure 7 the intensity of the HI large-sample discussed in Section 3.3 (and presented in Figure 6 for the ideal case) is plotted as a function of the retarded-time τ for the special case where dephasing/relaxation effects are included and characterized by a single time-scale set to $T' = 541 T_R$ (see Sections 4 and Appendix B). These results were obtained by once again numerically solving Equation (54), while the magnetization and population inversion are given by

$$\hat{\mathcal{M}}_0^+ = \frac{\mu_B N}{2\sqrt{2}V} \sin(\theta) e^{-\tau/T'} \quad (59)$$

$$\hat{N} = \frac{N}{V} \cos(\theta) e^{-\tau/T'}, \quad (60)$$

and the dimensionless parameter

$$q = 2\sqrt{\frac{z\tau'}{LT_R}} \quad (61)$$

with

$$\tau' = T' \left(1 - e^{-\tau/T'} \right). \quad (62)$$

The magnetic field is once again given by Equation (53). The intensity and time axes are scaled as those of Figure 6 for the ideal HI sample. We can see from Figure 7 that the ringing effect seen in the ideal sample is also present here but is weakened by the dephasing and basically terminated after $\tau \sim 1000 T_R$ (i.e., approximately the dephasing time-scale). The dephasing effects also affect the maximum energy radiated away through each burst event, and result in slightly weaker intensities.

4. Discussion - Cooperative Behavior in a HI Gas in the ISM

As was made evident from our previous discussions, the characteristic time-scale of superradiance T_R is a fundamental criterion to consider in the investigation of this cooperative behavior. For an ideal small-sample of volume $\mathcal{V} < \lambda^3 \sim 10^4 \text{ cm}^3$, for total hydrogen densities $1 \text{ cm}^{-3} < n_H < 100 \text{ cm}^{-3}$ and a population inversion $\eta \sim 0.01$, the superradiance time-scale

$$T_R = \frac{\tau_{\text{sp}}}{\eta n_H \mathcal{V}}, \quad (63)$$

$$\sim \frac{10^{12}}{n_H} \text{ s} \quad (64)$$

is such that $T_R \sim 10^{10} - 10^{12}$ sec, where $\tau_{\text{sp}} \sim 10^{14}$ sec for the 21 cm line. As mentioned in Section 3.3.1, t_D ($\approx T_R$, in this case) must be shorter than the relaxation/dephasing time-scales in order

to allow the build-up of cooperative behaviors in the sample. In a typical HI gas, an important relaxation mechanism for an atom is collisional de-excitation, the rate for which is given by

$$\tau_{\text{coll}} = \frac{1}{n_{\text{H}} \kappa_{10}}. \quad (65)$$

Values for the collisional de-excitation rate coefficient κ_{10} for the hyperfine state $F = 1$ over a range of temperatures can be found in Zygelman (2005), and for $10 \text{ K} < T < 300 \text{ K}$ we find $\tau_{\text{coll}} \sim 10^8 - 10^{12} \text{ sec}$ for the previous range of atomic hydrogen densities¹. These collision rates become $\tau_{\text{coll}} \sim 10^7 - 10^{12} \text{ sec}$ when elastic collisions are considered (Irwin 2007). It can thus be seen that the expected collisional relaxation time-scales are likely to render superradiance unlikely for small HI sample, especially at higher temperatures. This suggests the investigation of larger samples containing more atoms.

Although in a large-sample the general cooperative behavior is weaker than the ideal Dicke superradiance, the greater number of atoms will reduce T_{R} , increase the radiation intensity, and make it more likely to observe the effect. However, it is also important to realize that not only must the condition $T_{\text{R}} < T'$ be realized for establishing superradiance, such that the non-coherent de-excitation does not become the dominant mechanism to release the energy of the system, but we must also ensure that $\tau_{\text{D}} < T'$ is verified since $\tau_{\text{D}} > T_{\text{R}}$ from Equation (58). In other words, the delay time needed to establish coherence in the sample must also be smaller than the dephasing time-scale.

As previously discussed in Section 3.2.2, an ideal cylindrical large-sample of volume $\mathcal{V} \gg \lambda^3$ will release much of the energy stored within it through a series of radiation bursts, the so-called ringing effect, with the first burst of radiation appearing after the delay time τ_{D} needed to establish coherence in the sample. The ringing effect is associated to the re-absorption and re-emission of radiation through the end-fire of a large-sample interacting with the radiation originating from other parts of the sample upstream of the end-fire. Although we have not included radiation loss through diffraction in our analysis, in Section 3.3.1 a more realistic case was discussed by considering the special case where dephasing/relaxation effects are included and characterized by a single time-scale T' . As was just mentioned, this time-scale must be longer than the delay time τ_{D} , which is proportional to T_{R} , in order to allow the build-up of coherent behavior and superradiance. Since the superradiance time-scale T_{R} of a large-sample, as given by Equation (48), is a function of inverted population density n and the sample length L , and it may seem, at first sight, that τ_{D} can always be set to a value smaller than all dephasing/relaxation time-scales in any system by increasing these two parameters. However, the length or the density of inverted atoms are limited by other important parameters such as the pumping time T_{P} over which the population inversion is achieved throughout

¹As was previously emphasized, although we focus on regions of the ISM where thermal equilibrium has not been reached, in what follows we adopt the usual prescriptions to determine time-scales due to collisions, which we expect to be the dominant dephasing phenomenon. The figures thus obtained will be overestimated and can be considered as worse case scenarios.

the sample. As we increase the length of the sample T_R and τ_D decrease, but on the other hand, it becomes necessary to achieve the population inversion over a larger length-scale. There are two types of pumping mechanisms available to achieve the population inversion in an atomic system: swept pumping and instantaneous pumping (MacGillivray & Feld 1981; Gross & Haroche 1982). In the swept pumping scenario the atomic sample is pumped longitudinally by a pulse traveling along the sample, and the pumping process is characterized by a finite pumping time T_P , whereas for instantaneous pumping a transverse excitation causes the simultaneous excitation of all atoms in the sample resulting in $T_P \approx 0$. In our analyses of a small- or a large-sample, we assumed the instantaneous excitation of atoms in the sample to calculate the output intensity. When the pumping process cannot be achieved instantaneously, but is realized over a finite time, our results for the output intensity of a small- or a large-sample are only affected slightly as long as $T_P < \tau_D$. The main effect of the finite pumping time is then an increase in the delay time of the superradiant process in comparison to what one expects from Equation (48), i.e., the actual delay time τ'_D will be longer than the theoretical delay time τ_D (MacGillivray & Feld 1981).

However, if pumping occurs at an approximately constant rate over some time interval in a HI gas (i.e., $dn(t)/dt \simeq \Lambda$, where Λ is a constant) and the first burst of superradiant radiation is emitted before the expected inversion density n is achieved throughout the sample, then we need to replace n by its effective value at time $t = \tau'_D$ (i.e., $n_{\text{eff}} = n(\tau'_D)$). In this case, only a fraction of atoms contribute to the first burst, and the system cannot emit as much of the energy stored within it through a series of coherent bursts (MacGillivray & Feld 1981). If the pumping time becomes too long and the first superradiant burst is emitted before the inversion is achieved along the sample, only a few coherent bursts can be observed. This happens as the system reaches a quasi-steady state, in which the growth and depletion of population occur with the same rates. In the quasi-steady state the radiation intensity is given by $I = \hbar\omega L(dn/dt)$, and is no longer proportional to N^2 (MacGillivray & Feld 1981). The transition from a superradiant to the quasi-steady regime was first observed in the laboratory by Gross et al. (1979). For an astronomical system, this would correspond to passing from a superradiant system to an astronomical (i.e., mirror-less) maser. We therefore conclude that in the ISM superradiance will not happen in a steady state regime, but will rather be characterized by strong variability in radiation intensities over time. One could, for example, conceive of an emitting region harboring a maser that would be episodically modulated with strong bursts of radiation due to superradiance, perhaps resulting from some radiative trigger or a sudden decrease in τ_D (from a corresponding increase in the inverted population, for example).

In a more general context, i.e., without limiting the discussion to the 21 cm line, it is also important to note that superradiance cannot result from a population inversion due to collisions alone. This is because of the undesirable consequences collisions have on the dephasing/relaxation of a sample. That is, if T_P is the pumping time due to collisions, then we know from our previous discussion that $T_P < \tau_D$ for superradiance to be possible. But since in this case the time-scale for collision dephasing is $T' = T_P$ it follows that $\tau_D > T'$ and superradiance will be inhibited by collisions.

When $N \gg 1$ we have for the average delay time $\langle \tau_D \rangle = T_R \ln(N)$ (Gross & Haroche 1982), which means that $\langle \tau_D \rangle$ is usually an order of magnitude or two larger than T_R for the large-samples to be studied. As we will now see, for the range of densities and temperatures considered for our analysis $\langle \tau_D \rangle < T'$ can be realized in a large set of conditions. In a HI large-sample where all the necessary conditions for superradiance are fulfilled (i.e., $T_P, \tau_E < \langle \tau_D \rangle < T'$, with sufficient velocity coherence), we can estimate the time-scale of potential superradiance bursts using the results of our numerical analyses for the corresponding large-sample, as long as the Fresnel number is kept close to unity. For the following examples we considered a density $n_H = 10 \text{ cm}^{-3}$ with an inversion factor $\eta = 0.01$, implying an inverted population of 940 atoms in a volume λ^3 . Our results indicate that radiation bursts over time-scales on the order of days (i.e., from Figure 7 a few hundred times $T_R = 10^3 \text{ sec}$, while $\langle \tau_D \rangle = 5.2 \times 10^4 \text{ sec}$) can be associated to cylindrical HI samples of length and radius $L \approx 10^{11} \text{ cm}$ and $w \approx 9 \times 10^5 \text{ cm}$, respectively, while bursts over time-scales on the order of **minutes** (i.e., $T_R = 1 \text{ sec}$ and $\langle \tau_D \rangle = 66 \text{ sec}$) to samples with $L \approx 10^{14} \text{ cm}$ (approximately equal to $6 \times 10^{-5} \text{ pc}$; see Storer & Sciama 1968) and $w \approx 3 \times 10^7 \text{ cm}$. In all cases, we have $T' \approx \tau_{\text{coll}} > \langle \tau_D \rangle$ over a wide range of conditions, ensuring that dephasing effects will not destroy atomic coherent behaviors, and we found $f \approx 10^{-4}$ (from Figure 7) with an efficiency factor Nf ranging from approximately 10^{12} to 10^{24} , from the shortest to the longest sample length L . These results imply a corresponding amplification factor of 10^{10} to 10^{22} over the corresponding non-coherent intensity of such samples (taking into account the non-inverted population).

Although the samples considered above would probably not yield strong detections (e.g., for the sample of length $L \approx 10^{14} \text{ cm}$ and $w \approx 9 \times 10^7 \text{ cm}$ we calculate an integrated flux $\sim 10^{-22} \text{ erg s}^{-1} \text{ cm}^{-2}$ at a distance of 400 pc), given the small radii considered here it is unlikely that only a single superradiant system would be realized in a region harboring an inverted population. That is, if we assume a reasonable maser spot size for the population inverted region (e.g., $w_{\text{spot}} \sim 1 \text{ AU}$), then it becomes possible that a very large number of superradiant system could simultaneously erupt ($w_{\text{spot}}/w \sim 10^5$) and render a strong detection more likely, when the conditions for superradiance are met (Rajabi & Houde 2016). This leads us to suggest that despite the simplicity of, and the approximations used in, our model significant intensity variability due to superradiance could be detectable for the 21 cm line in some regions of the ISM, in view of the relatively low levels of population inversion required over the short astronomical length-scales considered here.

5. Conclusion

We have applied the concept of superradiance introduced by Dicke (1954) to the ISM by extending the corresponding analysis to the magnetic dipole interaction characterizing the atomic hydrogen 21 cm line. Although it is unlikely that superradiance could take place in thermally relaxed regions, in situations where the conditions necessary for superradiance are met (i.e., close atomic spacing, high velocity coherence, population inversion, and long dephasing time-scales compared to the those related to coherent behavior), our results suggest that relatively low levels of population inversion

over short astronomical length-scales (e.g., as compared to those required for maser amplification) can lead to the cooperative behavior required for superradiance in the ISM. Given the results of our analysis, we expect the observational properties of superradiance to be characterized by the emission of high intensity, spatially compact, burst-like features potentially taking place over short periods ranging from minutes to days.

As this first paper on this topic has, in part, served as an introduction to superradiance in the ISM, much remains to be done. For example, we have not attempted to characterize the shapes of superradiant spectral lines or their polarization properties, which for the 21 cm line would necessitate the consideration of all hyperfine $F = 1 \leftrightarrow 0$ transitions. In subsequent publications, we thus intend to extend our analysis to tackle these questions and investigate the potential for superradiance in other important astronomical spectral lines. It would further be beneficial to broaden the scope of our analysis to include a wider range of conditions such effects as pumping, diffraction losses, and different sample geometries associated to different Fresnel numbers.

We thank M. Harwit for bringing this research topic to our attention, and J. Zmuidzinas for helpful discussions. M.H.’s research is funded through the NSERC Discovery Grant and the Canada Research Chair programs.

A. Theoretical Model

As discussed in Section 3.1, the Hamiltonian of the HI-sample system interacting with the 21 cm line via the $(F, m_F : 0, 0 \longleftrightarrow 1, +1)$ transition is

$$\hat{H} = \hbar\omega_0 \sum_{j=1}^N \left(\hat{R}_{j3} + \frac{\hat{1}}{2} \right) + \hat{H}_{\text{rad}} + \frac{\mu_B}{\sqrt{2}c} \sum_{\mathbf{k}} \sqrt{\frac{\hbar\omega_{\mathbf{k}}}{2\epsilon_0 V}} \sum_{j=1}^N \left(\hat{R}_j^+ \hat{a}_{L\mathbf{k}} e^{i\mathbf{k}\cdot\mathbf{r}_j} + \hat{R}_j^- \hat{a}_{L\mathbf{k}}^\dagger e^{-i\mathbf{k}\cdot\mathbf{r}_j} \right), \quad (\text{A1})$$

where we neglected any inhomogeneous broadening effect (i.e., we omit \hat{H}_0 and set $\omega_j = \omega_0$). The radiation Hamiltonian term \hat{H}_{rad} can be expressed in terms of the second quantized operators $\hat{a}_{L\mathbf{k}}$ and $\hat{a}_{L\mathbf{k}}^\dagger$, and $\hat{a}_{R\mathbf{k}}$ and $\hat{a}_{R\mathbf{k}}^\dagger$ associated to left- and right-circular polarized radiation states, respectively, with

$$\hat{H}_{\text{rad}} = \hbar\omega \sum_{\mathbf{k}} \left[\left(\hat{a}_{L\mathbf{k}}^\dagger \hat{a}_{L\mathbf{k}} + \frac{\hat{1}}{2} \right) + \left(\hat{a}_{R\mathbf{k}}^\dagger \hat{a}_{R\mathbf{k}} + \frac{\hat{1}}{2} \right) \right]. \quad (\text{A2})$$

The evolution of the atomic system can be discussed using the Heisenberg equation of motion for the operator \hat{X} in a system described by the Hamiltonian \hat{H} ,

$$\frac{d\hat{X}}{dt} = \frac{1}{i\hbar}[\hat{X}, \hat{H}]. \quad (\text{A3})$$

One can then readily find the following equations of motions for \hat{R}^+ , \hat{R}^- and \hat{R}_3 :

$$\frac{d\hat{R}^+}{dt} = i\omega_0\hat{R}^+ - \frac{i\sqrt{2}\mu_B}{\hbar}\hat{R}_3\hat{B}_L^- \quad (\text{A4})$$

$$\frac{d\hat{R}^-}{dt} = -i\omega_0\hat{R}^- + \frac{i\sqrt{2}\mu_B}{\hbar}\hat{R}_3\hat{B}_L^+ \quad (\text{A5})$$

$$\frac{d\hat{R}_3}{dt} = -\frac{i\mu_B}{\sqrt{2}\hbar}(\hat{R}^+\hat{B}_L^+ - \hat{R}^-\hat{B}_L^-), \quad (\text{A6})$$

where, for simplicity, we now set \hat{B}_L^\pm for the value of the LCP-component of the magnetic field averaged over the positions of the atoms. In a similar way, we can write the following equations of motions for the raising and lowering magnetization operators $\hat{\mathcal{M}}^+(\mathbf{r})$ and $\hat{\mathcal{M}}^-(\mathbf{r})$ using Equation (28) as

$$\frac{d\hat{\mathcal{M}}^+}{dt} = -i\omega_0\hat{\mathcal{M}}^+ - \frac{i\mu_B^2}{\hbar}(\mathbf{e}_L \cdot \hat{\mathbf{B}}_L^+) \hat{R}_3 \mathbf{e}_L \quad (\text{A7})$$

$$\frac{d\hat{\mathcal{M}}^-}{dt} = i\omega_0\hat{\mathcal{M}}^- + \frac{i\mu_B^2}{\hbar}(\mathbf{e}_L^* \cdot \hat{\mathbf{B}}_L^-) \hat{R}_3 \mathbf{e}_L^*. \quad (\text{A8})$$

It is also useful to define the operator \hat{N}

$$\hat{N} = 2\hat{R}_3 \quad (\text{A9})$$

$$= 2 \sum_{j=1}^N \hat{R}_{3j} \delta(\mathbf{r} - \mathbf{r}_j), \quad (\text{A10})$$

which can be interpreted as a population inversion density operator considering that \hat{R}_{3j} has eigenvalues of $\pm 1/2$ and the eigenvalue of $\hat{R}_3 = \sum \hat{R}_{3j}$ is equal to half of the population difference between the excited level $F = 1, m_F = 1$ and the ground level $F = 0, m_F = 0$ at time t . Using Equations (A6) and (A10), one can show that the time evolution of the population inversion obeys

$$\frac{d\hat{N}}{dt} = \frac{2i}{\hbar}(\hat{\mathcal{M}}^+ \cdot \hat{\mathbf{B}}_L^+ - \hat{\mathcal{M}}^- \cdot \hat{\mathbf{B}}_L^-). \quad (\text{A11})$$

Using Equation (A10), Equations (A7) and (A8) can be rewritten in the following form of

$$\frac{d\hat{\mathcal{M}}^+}{dt} = -i\omega_0\hat{\mathcal{M}}^+ - i\gamma(\mathbf{e}_L \cdot \hat{\mathbf{B}}_L^+) \hat{\mathbf{N}}\mathbf{e}_L \quad (\text{A12})$$

$$\frac{d\hat{\mathcal{M}}^-}{dt} = i\omega_0\hat{\mathcal{M}}^- + i\gamma(\mathbf{e}_L^* \cdot \hat{\mathbf{B}}_L^-) \hat{\mathbf{N}}\mathbf{e}_L^*, \quad (\text{A13})$$

where $\gamma = \mu_B^2/2\hbar$.

Furthermore, in the Heisenberg representation one can derive the following equation

$$-\nabla^2\hat{\mathbf{B}}_L^\pm + \frac{1}{c^2}\frac{\partial^2\hat{\mathbf{B}}_L^\pm}{\partial t^2} = -\mu_0\nabla^2\hat{\mathcal{M}}^\pm \quad (\text{A14})$$

for the evolution of the magnetic component of the radiation field when defining

$$\hat{B}_L^\pm(\mathbf{r}, t) = \hat{B}_0^\pm(\mathbf{r}, t) e^{\pm i(kz - \omega t)} \quad (\text{A15})$$

$$\hat{\mathcal{M}}^\pm(\mathbf{r}, t) = \hat{\mathcal{M}}_0^\pm(\mathbf{r}, t) e^{\pm i(kz - \omega t)}, \quad (\text{A16})$$

using the slowly varying envelope approximation (SVEA), where \hat{B}_0^\pm and $\hat{\mathcal{M}}_0^\pm$ are slow varying envelope operators multiplied by fast oscillating exponential terms propagating in the positive z direction. Within the context of the SVEA we assume that the \hat{B}_0^\pm and $\hat{\mathcal{M}}_0^\pm$ significantly change over time-scales much longer than $1/\omega$ and length-scales much larger than $1/k$ (Gross & Haroche 1982). This assumption is justified by the fact that the variation of the complex field $\hat{B}_L^\pm(\mathbf{r}, t)$ is related to atomic variations, which occurs over time-scales and spatial-scales, respectively, much larger than the period and wavelength associated with the radiation (Mandel 2010). Upon applying the SVEA, Equation (A14) is simplified to

$$\left(\frac{\partial}{\partial z} + \frac{1}{c}\frac{\partial}{\partial t}\right)\hat{B}_0^\pm \simeq \pm \frac{i\mu_0\omega}{2c} \langle \hat{\mathcal{M}}_0^\pm \rangle. \quad (\text{A17})$$

In the derivation of Equation (A17), we neglected any transverse effects on the radiation field and magnetization (i.e., $\partial B_0^\pm/\partial x \approx \partial B_0^\pm/\partial y \approx 0$ and $\partial \hat{\mathcal{M}}_0^\pm/\partial x \approx \partial \hat{\mathcal{M}}_0^\pm/\partial y \approx 0$), which should be included in numerical calculations for a true three-dimensional sample.

Using Equations (A15) and (A16) we can rewrite Equations (A11), (A12), and (A13) at resonance, i.e., when $\omega = \omega_0$, in the reduced form of

$$\frac{d\hat{\mathcal{M}}_0^\pm}{dt} = \mp i\gamma\hat{B}_0^\pm \hat{\mathbf{N}} \quad (\text{A18})$$

$$\frac{d\hat{\mathbf{N}}}{dt} = \frac{2i}{\hbar} (\hat{\mathcal{M}}_0^- \hat{B}_0^+ - \hat{\mathcal{M}}_0^+ \hat{B}_0^-). \quad (\text{A19})$$

Equations (A17), (A18) and (A19) are known as the Maxwell-Bloch equations, and can be solved simultaneously to determine the time evolution of the radiation field, the magnetization, and the excitation state for an ideal sample.

A.1. Dephasing Effects and Pumping

The previous derivations for the ideal case must be augmented appropriately when dealing with more realistic conditions for the ISM, where dephasing and relaxation effects cannot be neglected and continuous pumping of the atomic system can take place. One can phenomenologically add the corresponding terms to the atomic equations as follows (Mandel 2010)

$$\frac{d\hat{\mathcal{M}}_0^+}{dt} = -i\gamma\hat{B}_0^+\hat{N} - \frac{1}{T_2}\hat{\mathcal{M}}_0^+ + \Lambda_M \quad (A20)$$

$$\frac{d\hat{N}}{dt} = \frac{2i}{\hbar} \left(\hat{\mathcal{M}}_0^- \hat{B}_0^+ - \hat{\mathcal{M}}_0^+ \hat{B}_0^- \right) - \frac{1}{T_1} \left(\hat{N} - N_{eq} \right), \quad (A21)$$

where T_1 and T_2 are the characteristic time-scales for, respectively, population decay and demagnetization, N_{eq} is the “equilibrium” value for \hat{N} obtained in the absence of interaction with the coherent field \hat{B}_L , while Λ_M represents any source term of magnetization. More precisely, the term $-\hat{N}/T_1$ is needed to reflect the finite life-time of the excited level $F = 1$, $m_F = 1$, and N_{eq}/T_1 is added to take into account all non-coherent processes that affect the atomic levels (e.g., pumping, absorption and stimulated emission processes). The finite life-time of the atomic excited level also results in the decay of magnetization for which $-\hat{\mathcal{M}}_0^+/T_2$ term accounts in Equation (A20). If we want to study the evolution of the atom-field system over long periods of time, we need to include the magnetization pumping term Λ_M to have a continuous source of magnetization to counteract the effect of the $-\hat{\mathcal{M}}_0^+/T_2$ term (Benedict et. al. 1996).

The magnetic field Equation (A17) can also be adapted to the more realistic conditions by adding a correction term to account for the loss of radiation due to transverse effects and diffraction, which depend on the shape and symmetry of the sample. These are characterized by the Fresnel number

$$F = \frac{A}{\lambda L}, \quad (A22)$$

where A and L , respectively, stand for the cross-section and length of the sample. For samples of cylindrical symmetry with Fresnel number smaller than one, transverse effects of the field are negligible, whereas the diffraction of radiation along the propagation axis can play an important role. Gross & Haroche (1982) have shown that a damping term B_0^+/L_{diff} can be included in the field equation to take into account diffraction effects in samples with $F \ll 1$. For such a sample Equation (A17) can be approximately augmented to

$$\left(\frac{\partial}{\partial z} + \frac{1}{c} \frac{\partial}{\partial t} \right) \hat{B}_0^+(z, \tau) + \frac{1}{L_{diff}} B_0^+(z, \tau) \simeq \frac{i\mu_0\omega}{2c} \hat{\mathcal{M}}_0^+, \quad (A23)$$

where $L_{\text{diff}} \simeq FL/0.35$ (Gross & Haroche 1982).

The atom-field Equations (A21), (A20) and (A23) also form a Maxwell-Bloch system of equations, and provide a more complete and realistic picture for the evolution of the system. This set of equations can be numerically solved for a given set of parameters T_1 , T_2 , N_0 , N_{eq} and Λ_M . The numerical results for these equations will be discussed in a subsequent paper.

B. The Sine-Gordon Solution

The set of Equations (A20), (A21) and (A23) cannot be solved analytically (Mandel 2010), and in general numerical techniques need to be developed to determine the output radiation intensity as a function of time. We thus first consider the ideal case, where the dephasing/relaxation, diffraction, and pumping terms are neglected (i.e., $T_1 = T_2 = \infty$, $L_{\text{diff}} = \infty$, and $\Lambda_M = 0$). Effecting a change of variable from t to the retarded time $\tau = t - z/c$ yields

$$\left(\frac{\partial}{\partial z} + \frac{1}{c} \frac{\partial}{\partial t} \right) = \frac{\partial}{\partial z} \quad (B1)$$

$$\frac{\partial}{\partial t} = \frac{\partial}{\partial \tau}, \quad (B2)$$

which can be used to simplify the set of Maxwell-Bloch equations (A17), (A18) and (A19). In this case we have

$$\frac{\partial \hat{\mathcal{M}}_0^\pm}{\partial \tau} = \mp i\gamma \hat{B}_0^\pm \hat{N} \quad (B3)$$

$$\frac{\partial \hat{N}}{\partial \tau} = \frac{2i}{\hbar} \left(\hat{\mathcal{M}}_0^- \hat{B}_0^+ - \hat{\mathcal{M}}_0^+ \hat{B}_0^- \right) \quad (B4)$$

$$\frac{\partial \hat{B}_0^\pm(z, \tau)}{\partial z} \simeq \pm \frac{i\mu_0\omega}{2c} \hat{\mathcal{M}}_0^\pm, \quad (B5)$$

which are more suitable for our purposes.

The form of Equations (B3) and (B4) implies that $|\hat{\mathcal{M}}^+|^2 + |\hat{\mathcal{M}}^-|^2 + (\mu_B^2/4) |\hat{N}|^2$ is a conserved quantity and allows us to redefine $\hat{\mathcal{M}}_0^\pm$ and \hat{N} as

$$\hat{\mathcal{M}}_0^+ = \frac{\mu_B N}{2\sqrt{2}V} \sin(\theta) \quad (B6)$$

$$\hat{N} = \frac{N}{V} \cos(\theta), \quad (B7)$$

where N is the number of inverted atoms in the sample at $\tau = 0$ and θ is the so-called Bloch angle.

Taking these solutions into account, at resonance Equations (B3) and (B5) are transformed to

$$\hat{B}_0^+ = \frac{i\mu_B}{2\sqrt{2}\gamma} \frac{\partial\theta}{\partial\tau} \quad (B8)$$

$$\frac{\partial\hat{B}_0^+}{\partial z} = \frac{i\mu_0\omega\mu_B N}{4\sqrt{2}cV} \sin(\theta) \quad (B9)$$

in the retarded-time frame. Taking the spatial derivative of Equation (B8) we can write

$$\frac{\partial\hat{B}_0^+}{\partial z} = \frac{i\mu_B}{2\sqrt{2}\gamma} \frac{\partial^2\theta}{\partial z\partial\tau}, \quad (B10)$$

which when compared to Equation (B9) yields the following non-linear equation

$$\frac{\partial^2\theta}{\partial z\partial\tau} = \frac{\mu_0\mu_B^2\omega N}{4\hbar cV} \sin(\theta) \quad (B11)$$

upon using $\gamma = \mu_B^2/2\hbar$. This equation is further transformed with the introduction of a new dimensionless variable (Gross & Haroche 1982)

$$q = 2\sqrt{\frac{z\tau}{LT_R}}, \quad (B12)$$

to

$$\frac{d^2\theta}{dq^2} + \frac{1}{q} \frac{d\theta}{dq} = \sin(\theta), \quad (B13)$$

with T_R the characteristic time for superradiance given by Equation (48). Equation (B13) is the so-called Sine-Gordon equation (Gross & Haroche 1982). This equation can be numerically solved and the corresponding solution for θ substituted back into Equation (B8) to determine the field amplitude \hat{B}_0^+ emerging out of the sample (at $z = L$) as a function of the retarded time τ . Knowing $\hat{B}_0^+(L, \tau)$, the output radiation intensity I is given by

$$I = \frac{c}{2\mu_0} \left| \hat{B}_0^+ \right|^2. \quad (B14)$$

The more realistic (but special) case where dephasing/relaxation is included (i.e., $T' = T_1 = T_2 \neq \infty$, $L_{\text{diff}} = \infty$, and $\Lambda_M = N_{\text{eq}} = 0$) can be dealt with in a similar manner. We then have the corresponding definitions for Equations (B6) and (B7)

$$\hat{\mathcal{M}}_0^+ = \frac{\mu_B N}{2\sqrt{2}V} \sin(\theta) e^{-\tau/T'} \quad (B15)$$

$$\hat{N} = \frac{N}{V} \cos(\theta) e^{-\tau/T'}, \quad (B16)$$

which also lead to Equation (B8) for \hat{B}_0^+ . Performing a spatial derivative on Equation (B8) yields

$$\frac{\partial^2 \theta}{\partial z \partial \tau} = \frac{\mu_0 \mu_B^2 \omega N}{4\hbar c V} \sin(\theta) e^{-\tau/T'}. \quad (B17)$$

A comparison of Equations (B17) with (B11) shows that the presence of dephasing implies a source term containing a decaying exponential. This exponential factor can be removed from this equation through the following change of variable

$$\tau \longrightarrow \tau' = T' \left(1 - e^{-\tau/T'} \right), \quad (B18)$$

which allows us to transform Equation (B17) to the Sine-Gordon equation (i.e., Equation (B13)) by redefining the dimensionless parameter q with the following

$$q = 2\sqrt{\frac{z\tau'}{LT_R}}. \quad (B19)$$

REFERENCES

Abel, N. P., Ferland, G. J., O'Dell, C. R., Shaw, G., & Troland, T. H. 2006, ApJ, 644, 344

Andreev, A. V., Emel'yanov, V. I., & Il'inskiĭ, Y. A. 1980, Physics-Uspekhi, 23(8), 493

Benedict, M. G., Ermolaev, A. M., Malyshev, V. A., Sokolov, I. V., & Trifonov, E. D., 1996, Super-radiance Multatomic Coherent Emission, IOP Publishing Ltd

Bonifacio, R. & Lugiato, L. A. 1975, Phys. Rev. A, 11(5), 1507

Carlson, N. W., Jackson, D. J., Schawlow, A. L., Gross, M., & Haroche, S., 1980, Opt. Commun., 32, 350-4

Cohen-Tannoudji, C., Diu, B., & Laloë, F., 1977, Mécanique Quantique (Paris: Hermann)

Condon & Shortley 1935, The Theory of Atomic Spectra (Cambridge: Cambridge)

Crutcher, R. M. 2012, ARA&A, 50, 29

Dicke, R. H. 1953, Phys. Rev., 89, 472

Dicke, R. H. 1954, Phys. Rev., 93, 99

Dicke, R. H. 1964, Quantum electronics, 1, 35-54

Draine, B. T. 2011, Physics of the interstellar and intergalactic medium, Princeton University Press (New Jersey: Princeton)

Dykstra, M., & Loeb, A. 2007, New Astronomy, 13, 395

Emerson, D. 1996, Interpreting Astronomical Spectra (New York: Wiley)

Field, G. B., 1958, Proceedings of the IRE, 46(1), 240

Fish, V. L. 2007, in Astrophysical Masers and their Environments, Proceedings of the International Astronomical Union, IAU Symposium, Vol. 242, 71

Furlanetto, S. R., & Furlanetto, M. R. 2007, MNRAS, 374(2), 547

Gibbs, H. M., Vrehen, Q. H. F., Hikspoors, H. M. 1977, Phys. Rev. Lett., 39, 547

Goldsmith, P. F., & Langer, W. D. 1999, ApJ, 517, 209

Greiner, C., Boggs, B., & Mossberg, T. W. 2000, Phys. Rev. Lett., 85, 3793

Gross, M., Goy, P., Fabre, C., Haroche, S., & Raimond, J. M. 1979, Phys. Rev. Lett., 43, 343

Gross, M. & Haroche, S. 1982, Physics Reports, 95(5), 301

Gross, M., Fabre, C., Pillet, P., Haroche, S. 1976, Phys. Rev. Lett., 36, 1035

Grynberg, G., Aspect, A., & Fabre, C. 2010, Introduction to Quantum Optics: from the Semi-classical Approach to Quantized Light, (Cambridge: Cambridge)

Irwin, J. A. 2007, Decoding the Cosmos (Chichester: Wiley)

Jackson, J. D. 1999, Classical Electrodynamics (New York: Wiley)

Kida, S. U. M. I. K. O., Niinuma, K., Suzuki, S., Tanaka, T., Nakanura, R., Takefuji, K. & Daishido, T., 2008 , New Astronomy, 13(7), 519-525.

MacGillivray, J. C. & Feld, M. S. 1981, Phys. Rev. A, 23(3), 1334

MacGillivray, J. C. & Feld, M. S. 1976, Phys. Rev. A, 14(3), 1169

Mandel, P., 2010, Nonlinear Optics, Wiley-VCH (Weinheim: Wiley-VCH)

Meath, W. J. 2004, J. Chem. Phys., 45(12), 4519

Meziane, J., Oullemine, S., Amezian, K., & Boursey, E. 2002, Chemical Physics Letters, 363(5), 573

Moi, L., Goy, P., Gross, M., Raimond, J. M., Fabre, C., Haroche, S. 1983, Phys. Rev. A, 27, 2043

Nussenzveig, H. M. 1973, Introduction to quantum optics, (New York: Gordon and Breach)

Protsenko, I. E. 2006, J. of Russian Laser Research, 27, 414

Rajabi, F. & Houde, M. 2016, ApJ, *submitted*

Rohlfs, K., & Wilson, T. L., Tools of Radio Astronomy, 4th rev. and enl. (Berlin: Springer)

Rosenberger, A. T., & DeTemple, T. A. 1981, Phys. Rev. A, 24, 868

Sarma A. P. 2012, in Cosmic Masers - from OH to H₀, Proceedings of the International Astronomical Union, IAU Symposium, Vol. 287, 41

Shklovskii, I. S. 1967, Sov. Astron., 11, 240

Skribanowitz, N., Herman, I. P., MacGillivray, J. C., and Feld, M. S. 1973, Phys. Rev. Lett., 30, 309

Stahler, S. W., & Palla, F. 2008, The Formation of Stars (Weinheim: Wiley-VCH)

Storer, S. H., & Sciama, D. W. 1968, Nature, 217, 1237

Townes, C. H., & Schawlow, A. L., Microwave Spectroscopy (New York: McGraw Hill-Book Co)

Vlemmings, W. H. T. 2012, in Cosmic Masers - from OH to H₀, Proceedings of the International Astronomical Union, IAU Symposium, Vol. 287, 54

Watson, W. D. 2009, RevMexAA, Conf. Ser., 36, 113

Wittke, J. P., & Dicke, R. H. 1956, Physical Review, 103(3), 620

Xia, H., Svidzinsky, A. A., Yuan, L., Lu, C., Suckewer, S., Scully, M. O. 2012, Phys. Rev. Lett., 109, 093604.

Zygelman, B. 2005, ApJ, 622, 1356